Mechanisms behind the Springtime North Pacific ENSO Teleconnection Bias in Climate Models𝒫

Ruyan Chen,[a,b] Isla R. Simpson,[c] Clara Deser,[c] Bin Wang,[b,d] and Yan Du[a]

[a] *State Key Laboratory of Tropical Oceanography, South China Sea Institute of Oceanology, Chinese Academy of Science, Guangzhou, China*
[b] *Ministry of Education Key Laboratory for Earth System Modeling and Department of Earth System Science, Tsinghua University, Beijing, China*
[c] *National Center for Atmospheric Research, Boulder, Colorado*
[d] *State Key Laboratory of Numerical Modeling for Atmospheric Sciences and Geophysical Fluid Dynamics, Institute of Atmospheric Physics, Chinese Academy of Sciences, Beijing, China*

ABSTRACT: Previous studies have shown that models overestimate the strength of ENSO teleconnections to the North Pacific during springtime, but the underlying reasons for this bias remain unknown. In this work, the relative contributions from basic-state and thermodynamic/dynamic forcing factors are disentangled through idealized experiments with the Community Earth System Model and a range of stationary wave modeling experiments. It is revealed that in CESM1 the diabatic heating biases over the tropical Indian Ocean and tropical central-western Pacific jointly favor a cyclonic (anticyclonic) circulation bias to occur in the North Pacific during the springtime of El Niño (La Niña) events. On one hand, the difference in the modeled and observed climatological basic state does not lead to the bias formation directly, as the diabatic heating biases are the primary cause. On the other hand, the springtime basic state is conducive to a more vigorous stationary wave response to the biased diabatic heating than the wintertime state, and this explains why the teleconnection bias occurs during springtime but not in winter. An iterative bias-correction approach is then implemented in the atmospheric model component of CESM1 to verify the linkage between the tropical diabatic heating bias and the teleconnection bias. Moreover, this explanation is shown to be relevant in other models of phase 5 of the Coupled Model Intercomparison Project (CMIP5) as a strong relationship is found between biases in ENSO-related tropical central-western Pacific/Indian Ocean precipitation and North Pacific circulation across models in spring.

SIGNIFICANCE STATEMENT: The purpose of this study is to explain why climate models tend to overestimate the springtime ENSO teleconnection to the North Pacific. Through both simplified and comprehensive model experiments, we found that the diabatic heating biases over the tropical Indian Ocean and central-western Pacific basins are the main cause behind the circulation bias. Although similar heating biases also occur in winter, the spring mean climate state is more sensitive to the biased heating than the winter mean state. These findings are useful for developing future climate models that would better simulate the springtime climate response during the ENSO events, as the same problem can be found in many other models.

KEYWORDS: Atmospheric circulation; ENSO; Teleconnections; Climate models; Bias; Spring season

1. Introduction

El Niño–Southern Oscillation (ENSO) is the most prominent ocean–atmosphere coupled mode of tropical interannual variability (Bjerknes 1969; McPhaden et al. 2006). Through the modulation of tropical convection, ENSO-related sea surface temperature (SST) anomalies induce a large-scale atmospheric circulation response (e.g., Horel and Wallace 1981; Held and Kang 1987; Zhang et al. 1996; Seager et al. 2003; L'Heureux and Thompson 2006; Deser et al. 2017; Domeisen et al. 2019), which has a profound global climate impact (e.g.,

Ropelewski and Halpert 1986; Trenberth et al. 2002; Lyon and Barnston 2005; Cai et al. 2011; Deser et al. 2018). These ENSO-triggered anomalous atmospheric circulation patterns are usually called "ENSO teleconnections" due to their remote influence, far from the SST anomalies that drive them. Many different aspects of the ENSO teleconnection patterns have now been discovered (Horel and Wallace 1981; Karoly 1989; Ghil and Mo 1991; Wang et al. 2000), among which the North Pacific ENSO teleconnection is perhaps the most important pathway through which the influence of ENSO is transmitted to the middle and high latitudes of the Northern Hemisphere (Bjerknes 1966; Ropelewski and Halpert 1986; Kim et al. 2019; Herceg-Bulić and Kucharski 2012; Herceg-Bulić et al. 2017). During the warm (cold) phase of ENSO, the North Pacific ENSO teleconnection refers to the anomalous cyclonic (anticyclonic) circulation response centered over the North Pacific region. Although its intensity usually peaks in winter and decays in the following spring corresponding to the life cycle of ENSO

(Spencer and Slingo 2003; Chen et al. 2020), it should be noted that the potential predictability of its climate impact could be higher during spring because the background noise during that season is substantially reduced compared to midwinter (Kumar and Hoerling 1998). Moreover, some other studies have found that some anomalous weather events during springtime were likely linked to a prolonged influence from ENSO maturing in the previous winter (Wolter et al. 1999; Schmidt et al. 2001; Allen et al. 2015; Jong et al. 2016). Therefore, an accurate representation of the springtime North Pacific ENSO teleconnection in climate models is important for attribution and seasonal forecasting of anomalous weather/climate events due to ENSO.

While most prior studies that have examined model biases in ENSO teleconnections have focused on the winter months, Alexander et al. (2002) and Spencer and Slingo (2003) independently pointed out that the North Pacific circulation anomalies during the springtime of ENSO tend to be overestimated in models. A more recent assessment of models by Chen et al. (2020) further verified that this overly strong springtime North Pacific ENSO teleconnection bias can be ubiquitously detected in many different climate models (i.e., CMIP5/CMIP6) and different configurations (such as coupled, atmosphere-only, or pacemaker experiments). To rule out the possibility that the bias is purely caused by sampling error associated with internal variability, the significance was tested through a bootstrapping technique as introduced by Deser et al. (2017, 2018). As illustrated in Chen et al. (2020), the overly strong teleconnection signal during the springtime of ENSO in models can further bias the simulated climate influence over North America, manifested as an overly prolonged springtime ENSO effect. Furthermore, no relationship was found between the bias strength and model-top height, extratropical SST variability, atmospheric chemistry, biochemistry, or model resolution. At this stage, no explanation has been given for the origins of this springtime North Pacific ENSO teleconnection bias.

Based on stationary wave theory, the large-scale quasistationary wave pattern can be interpreted as a steady atmospheric response to anomalous wave source forcing under a specific climatic basic state (Ting and Sardeshmukh 1993; Sardeshmukh and Hoskins 1988; Ting and Yu 1998; Held et al. 2002). From this perspective, the fundamental question is to determine which part takes the greatest responsibility for the formation of the springtime North Pacific ENSO teleconnection bias. Is it biases in the tropical heating? Biases in the basic state that affect the wave source? Biases in the basic state that affect the wave propagation? Or biases in extratropical processes or feedbacks that may impact stationary wave formation and evolution? It is difficult to disentangle the different roles played by each factor through composite analyses alone. In this paper, we use a stationary wave (SW) model (Ting and Held 1989; Held et al. 2002) to identify the relative roles of tropical diabatic heating biases and basic-state biases in contributing to the ENSO teleconnection bias. We then apply an "iterative bias-correction" approach in a full general circulation model (GCM) to verify the conclusion indicated by the SW model. The potential cause of the "seasonal preference" of the bias (i.e., its tendency to occur exclusively during

the springtime) is also explored. The uniformity of the bias-formation mechanism in different climate models is addressed in a preliminary manner by multimodel regression.

The rest of this paper is organized as follows. Section 2 describes the data and models used. Section 3 presents the stationary wave modeling results for exploring the key factors behind the teleconnection bias. In section 4 an iterative bias-correction technique in the Community Atmosphere Model version 5 (CAM5) is introduced and its effectiveness at alleviating the ENSO teleconnection bias is discussed. A summary and discussion are provided in section 5.

2. Models and data used

a. Stationary wave model

1) MODEL INTRODUCTION

Stationary wave theory tells that the background state and anomalous forcing work together in determining the stationary wave response. To isolate the relative contributions of biases in the forcing, and biases in the basic-state circulation, in forming the springtime North Pacific ENSO teleconnection bias, a baroclinic stationary wave (SW) model is adopted in this paper (Ting and Yu 1998; Held et al. 2002). The SW model is based on the three-dimensional (3D) primitive equations and all the variables are described as deviations from the zonal mean. The model has rhomboidal wavenumber-30 truncation in the horizontal and 14 vertical σ coordinate levels. The time scale of the Rayleigh friction and Newtonian cooling is 15 days at all levels, and the biharmonic diffusion coefficient is set to 1×10^{17} m^4 s^{-1}. These dampings are necessary to reach a steady-state model solution. Given that this model produces a steady-state solution, it does not simulate transient eddy influence on the mean flow. Instead, the transient eddies' influence is prescribed via forcing terms. In our experiment design, anomalous diabatic heating and transient momentum flux during the ENSO years are added as the forcing terms onto the climatological three-dimensional basic state. Note that the contribution from orographic forcing is embedded in the basic state as the basic state is prescribed as the climatological 3D state as opposed to the zonal mean. Thus, nonlinearities between the orography and anomalous heating and transients are not represented. By integrating the model for a short period [usually after tens of days; in Ting and Yu (1998) about 30 days], the stationary wave response during ENSO can be obtained. Compared with an atmospheric general circulation model (AGCM), the SW model does not incorporate sophisticated physical processes and feedback mechanisms. However, the model has the capability of capturing the climatological large-scale stationary wave patterns, as well as depicting the anomalous response to tropical diabatic heating anomalies related to ENSO (Ting and Yu 1998; Held et al. 1989; Ting and Held 1989; Ting and Sardeshmukh 1993; Held et al. 2002; Jong et al. 2020). The stationary wave model is much easier to interpret than a full AGCM and provides the opportunity to pull apart the different contributions to stationary wave anomalies. It is also computationally inexpensive, which makes it practical to carry out a

large suite of sensitivity experiments to isolate the role played by different aspects. That being said, the lack of two-way interactions between the anomalous forcing and circulation response inevitably leads to its oversimplification of the response, and in some cases it can be challenging to isolate cause and effect, where feedbacks are involved. We, therefore, complement the stationary wave modeling approach with an iterative bias correction procedure within a comprehensive climate model.

2) DATA FOR RUNNING SW MODEL EXPERIMENTS

In this paper, the input fields for the SW model consist of two categories: observation-based and model-based. To calculate the observation-based input fields, the 55-year Reanalysis dataset JRA-55 provided by the Japan Meteorological Agency (JMA) is used (Kobayashi et al. 2015; Harada et al. 2016). This dataset provides high-quality climate reanalysis data spanning 1958 to the present. Based on the 4D-Var data assimilation scheme, a larger number of observational data sources are incorporated in JRA-55. It also has a relatively high spatial (T319 × 60 levels) and temporal resolution (6 hourly). To prepare the input fields for model-based simulations, the ensemble mean of a 10-member set of CESM1 Tropical Ocean–Global Atmosphere (TOGA) simulations is used based on the period 1958–2010. Following convention (e.g., Lau and Nath 1994; Trenberth et al. 1998), SSTs in the TOGA simulations are prescribed with observed time-evolving SSTs in the tropics (30°–30°N) and the observed climatological seasonal cycle elsewhere. The TOGA configuration has been widely adopted to study the model's response to the observed tropical SST evolutions, especially those related to ENSO (e.g., Deser et al. 2017; Thirumalai et al. 2017; Lehner et al. 2018).

The diabatic heating forcing needed by the SW model is calculated as the residual of the thermodynamic equation as follows:

$$Q = \frac{\partial T}{\partial t} + \mathbf{V} \cdot \nabla T - \omega\left(k\frac{T}{p} - \frac{\partial T}{\partial p}\right), \quad (1)$$

where Q stands for the diabatic heating and $\partial T/\partial t$ is the local temperature change; $-\mathbf{V} \cdot \nabla T$ and $\omega(kT/p - \partial T/\partial t)$ are the horizontal and vertical thermal advection term respectively, where T represents the air temperature, $\mathbf{V}$ is the horizontal winds vector, and ω is the vertical velocity in pressure coordinates; $k = R_d/C_p$, where R_d is the specific gas constant for dry air and equals 287 J kg^{-1} K^{-1}, and C_p is the specific heat at constant pressure, which equals 1004.7 J kg^{-1} K^{-1}. For calculating the observed diabatic heating, all the variables required by Eq. (1) are taken from JRA-55 monthly reanalyses. As a result, the heating transport by submonthly transients is included in the calculated field. It is reasonable to include the contribution from transients given that the SW model cannot simulate that effect independently (Held et al. 2002). Comparison with the Q calculated using 6-hourly data reveals major differences over the extratropical storm tracks. In the tropics, however, the heat flux convergence by submonthly transients is relatively small compared to the diabatic heating (not shown). We prefer to use the monthly

data to estimate the diabatic heating because not all necessary fields are available at a higher time resolution for the TOGA simulations, and it is a reasonable approach for the SW model. However, we caution that, although it is a good approximation for the tropical area, the extratropical "diabatic heating" presented in this paper will be greatly influenced by the transient heat flux convergence. To verify the reliability of the calculated diabatic heating based on JRA-55, other reanalysis data including NCEP–NCAR (R1) (Kalnay et al. 1996), ERA20C (Poli et al. 2016), ERA-Interim (Dee et al. 2011), ERA5 (Hersbach et al. 2020), and CFSR (Saha et al. 2010) are also used for comparison.

The convergence of the transient vorticity flux $(-\Delta\overline{\mathbf{V}'\zeta'})$ is used to represent the transient momentum forcing, where ζ represents the vorticity (Hurrell 1995; Ting and Yu 1998). The overbar represents a monthly average and the prime indicates fluctuations about the monthly mean. Assuming the continuity equation holds, $-\Delta\overline{\mathbf{V}'\zeta'}$ can be rewritten as $(\partial^2\overline{u'v'}/\partial x^2 - \partial^2\overline{u'u'}/\partial x\partial y + \partial^2\overline{v'v'}/\partial x\partial y - \partial^2\overline{u'v'}/\partial y^2) \times (-1)$, which allows it to be calculated from the monthly accumulated fluxes available from the TOGA output. The transient divergence flux convergence $(-\Delta\overline{\mathbf{V}'\text{div}'})$ is not included because it could not be straightforwardly calculated from the available TOGA data, and it is not an important forcing term in the reanalysis (not shown). For each SW modeling experiment, the model is integrated for 60 days, and the average of the last 20 days is used for analysis.

b. Community Atmosphere Model version 5

1) MODEL INTRODUCTION

Developed primarily at the National Center for Atmospheric Research (NCAR), the Community Atmosphere Model (CAM) is one of the most widely used global atmospheric models for weather and climate research (Danabasoglu et al. 2020). The latest release reaches version 6.3 (CAM6.3) within the framework of the Community Earth System Model, version 2 (CESM2) (Bogenschutz et al. 2018; Danabasoglu et al. 2020). To be consistent with the CESM1 TOGA simulations, the previous version, CAM5 (Neale et al. 2012), is adopted in this paper (Kay et al. 2015; Deser et al. 2018).

2) DATA FOR CAM5 SIMULATIONS

Two initial experiments are carried out using CAM5: 1) the control simulation (CTRL), in which the climatological SSTs are prescribed and taken from the 1800-yr preindustrial simulations of the CESM Large Ensemble Project (Kay et al. 2015), and 2) the El Niño SST forcing simulation (EN), in which the SST forcing is obtained by superimposing the composited SST anomalies (ERSSTv3b; Smith et al. 2008; 40°S–40°N) during El Niño events onto the CTRL's climatological SSTs. The El Niño events are defined when the DJF-mean Niño-3.4 index is greater than one standard deviation from the mean (Chen et al. 2020), and only the events during 1958–2010 (the overlapping period of TOGA and JRA-55) are selected. We branch off on 1 October of each year of CTRL and run an ensemble of 20 EN simulations from October to April. Therefore, the response to El Niño SST anomalies is
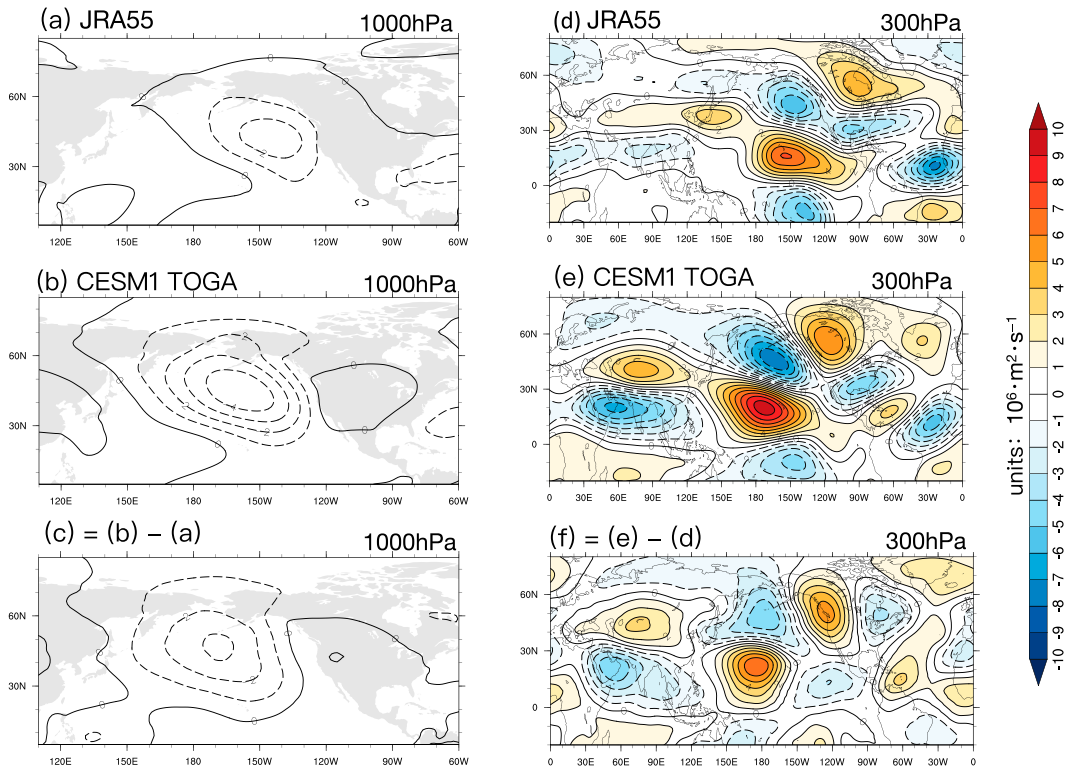
FIG. 1. Stationary wave components of the FM averaged (left) 1000- and (right) 300-hPa streamfunction anomalies of El Niño events during 1958–2010: (a),(d) the observational fields based on JRA-55, (b),(e) the outputs from TOGA simulations, and (c),(f) their difference.

available as the difference between the 20-member ensemble mean of the EN and CTRL simulations (this EN minus CTRL difference is referred to as "NINO" hereafter).

We then run a series of iterative bias-correction simulations using CAM5. The purpose of these bias-correction simulations is to artificially eliminate or alleviate the diabatic heating bias in the model by adding a correction term into the model integration process. The correction term is calculated from the difference between the observed (using JRA-55) and modeled diabatic heating fields. Technical details of applying the iterative bias-correction approach will be given in section 4.

c. Other model simulations and observational data

The precipitation and sea level pressure (SLP) fields simulated by the Coupled Model Intercomparison Project phase 5 (CMIP5) models' preindustrial (piControl) simulations are adopted for investigating the relationship between the tropical precipitation bias and the springtime North Pacific ENSO teleconnection bias across different models. The observed precipitation during 1979–2010 is taken from the Global Precipitation Climatology Project (GPCP) version 2 (Adler et al. 2003). The observed SLP is based on the European Centre for Medium-Range Weather Forecasts (ECMWF) twentieth-century reanalysis (ERA20C; Poli et al. 2016), in which surface pressure and winds are assimilated using ICOADS observations, and our conclusions would remain qualitatively unchanged if other reanalysis datasets were used instead (Chen et al. 2020). In this

paper, the springtime of ENSO specifically refers to the mean of February–March (FM) following the ENSO peaking winter, when the North Pacific circulation bias is most evident (Chen et al. 2020). Although the FM season is more often called the late-winter or early-spring, the term "springtime" is preferred in this work because it is a long-standing bias feature that was first discovered in the spring months' average (March–May), until Chen et al. (2020) pointed out that it is most significantly seen during February and March. So we continue to refer to the springtime bias for consistency with previous literature.

3. Stationary wave modeling results

a. Model validation

Figure 1 shows the stationary wave component (i.e., deviation from the zonal mean) of the streamfunction anomalies at 1000 and 300 hPa composited during FM of the El Niño spring in JRA-55 and CESM1 TOGA simulations separately. Their differences (i.e., the bias fields to be explained) are shown in Figs. 1c and 1f. The panels for the upper-level states (right column of Fig. 1) are colored and expanded in the display area to show the global stationary wave structure. In the lower troposphere near the surface, the North Pacific cyclonic circulation anomaly simulated by TOGA is significantly stronger than that in observation. In addition, a westward shift bias is noticeable for its central position (cf. Figs. 1a,b). In the

TABLE 1. Stationary wave modeling configurations for model validation and isolating the roles of anomalous forcing and basic state. The basic state is the FM climatology of winds, surface pressure, and temperature during 1958–2010. Diabatic heating and momentum forcing by the transients are composited anomalies during FM of the El Niño years.

Experiment	Basic state	Heating	Transients
JRA_all	JRA	JRA	JRA
TOGA_all	TOGA	TOGA	TOGA
TOGA_H+JRA_T+JRA_B	JRA	TOGA	JRA
JRA_H+TOGA_T+JRA_B	JRA	JRA	TOGA
JRA_H+JRA_T+TOGA_B	TOGA	JRA	JRA

upper troposphere, the observations exhibit a wave train structure propagating from the equatorial central Pacific to the mid- to high latitudes of the North Pacific and North America (Fig. 1d). In the TOGA simulations, the wave train structure is similar to that in observations but with a stronger amplitude. By differing the observed and modeled fields, the upper level exhibits a quadrupole bias pattern covering the North Pacific region (Fig. 1f).

The feasibility of using the SW model to trace the bias source relies on its ability to reproduce the above-displayed bias features. To test that, two independent simulations are carried out using the SW model (Table 1). One is the observation-based simulation ("JRA_all"), which means the basic state and anomalous forcing are all taken from the JRA-55. The other is the model-based simulation ("TOGA_all"), which means the corresponding fields needed by the SW model are derived from the CESM1 TOGA outputs. Specifically, the basic state refers to the February–March mean of the temperature, surface pressure, and horizontal wind fields during 1958–2010 based on either JRA-55 or CESM TOGA simulations, and the forcing terms are calculated by compositing the observed or modeled anomalous diabatic heating and transient momentum for the springtime (FM) of the El Niño years. The diabatic heating and transient forcing effects in the Southern Hemisphere and the Arctic regions are not included, but the modeling results would remain qualitatively unchanged if they are employed globally (not shown).

The modeling results shown in Fig. 2 indicate that the SW model can reproduce the fields shown in Fig. 1 reasonably well. For the lower-level circulation response (Figs. 2a–c), TOGA_all simulates a stronger cyclonic anomaly than JRA_all does over the North Pacific. The upper-level wave structures are also well captured by the SW model for both the observation-based (JRA_all; Fig. 2d) and the model-based (TOGA_all; Fig. 2e) simulations. Compared to the observed pattern, the teleconnection pattern simulated by the TOGA_all experiment is not only stronger but also extends westward (Figs. 2d,e). The quadrupole bias pattern covering the North Pacific region is also well reproduced by the SW
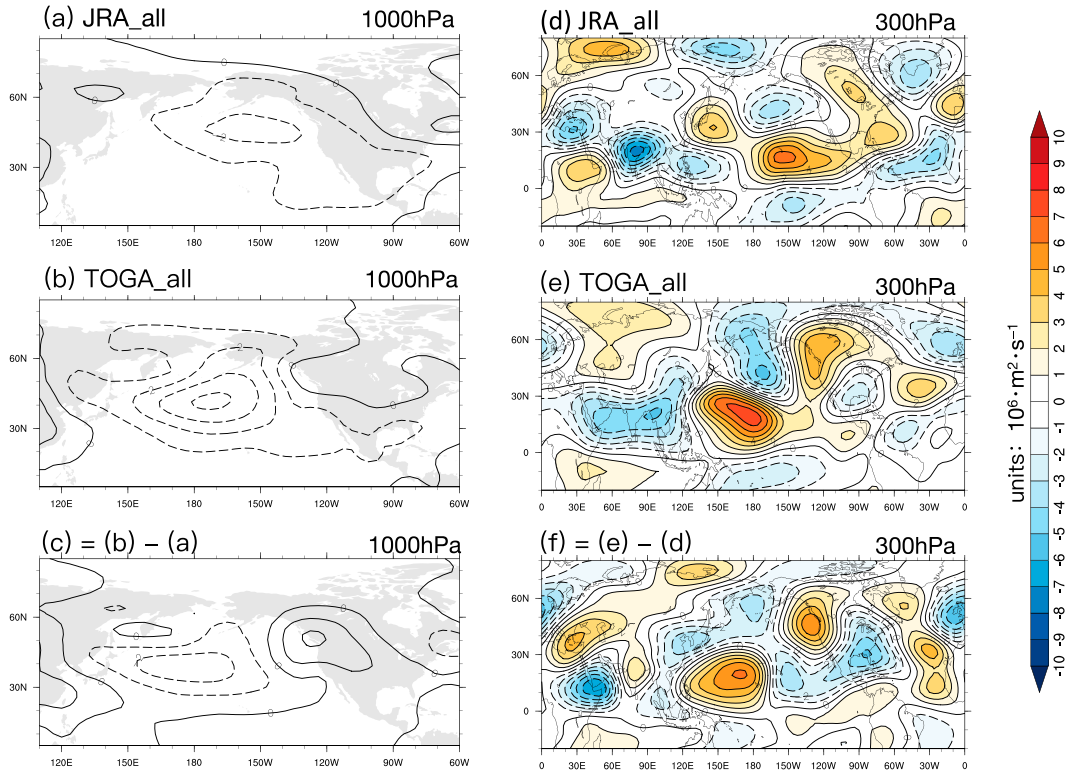

FIG. 2. Stationary wave components of the (left) 1000- and (right) 300-hPa streamfunction anomalies simulated by the (a),(d) JRA_all experiments and (b),(e) TOGA_all experiments in Table 1, and (c),(f) their difference.
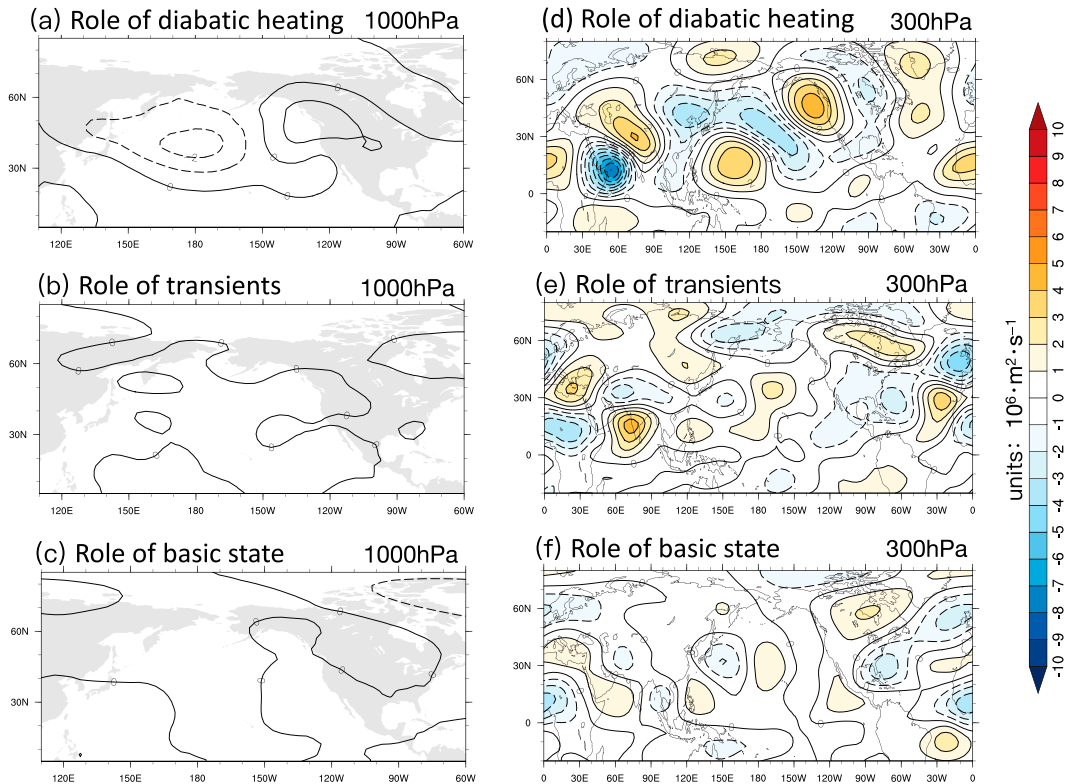
FIG. 3. Stationary wave components of the (left) 1000- and (right) 300-hPa streamfunction anomalies simulated by (a),(d) the difference between TOGA_H+JRA_T+JRA_B and JRA_all experiments for isolating the role of diabatic heating, (b),(e) the difference between JRA_H+TOGA_T+JRA_B and JRA_all experiments for isolating the role of transient momentum forcing, and (c),(f) the difference between JRA_H+JRA_T+TOGA_B and JRA_all experiments for isolating the role of basic state.

model as manifested in Fig. 2f. Therefore, the springtime North Pacific ENSO teleconnection bias in TOGA can be reproduced by the SW model to a great extent, although the amplitude of the biased cyclonic circulation over the North Pacific is a little weaker in the SW model. Substantial differences between the actual TOGA bias and the SW model bias can be seen in the north Indian Ocean–Asian region. Note that nonlinear interactions of the anomalous wave with the topography are not included, but we also tried starting from the zonal mean basic state and using the orography as an independent forcing component. The corresponding SW modeling results suggest that the nonlinear effects caused by the interactions with orography are negligible (not shown). We will use the stationary wave model to disentangle the relative contributions from anomalous forcing and basic state to the biased circulation response to El Niño in the next step.

b. Isolating the roles of anomalous forcing and basic state

To separate the relative contributions from basic-state biases and anomalous forcing biases in forming the springtime North Pacific ENSO teleconnection bias as reproduced by the TOGA_all experiment, three perturbation experiments are carried out: "TOGA_H+JRA_T+JRA_B", "JRA_H1TOGA_T1JRA_B",

and "JRA_H+JRA_T+TOGA_B" (Table 1). Based on JRA_all, only one component among the basic state [denoted by "(·)_B"], anomalous diabatic heating [denoted by "(·)_H"], and anomalous transient momentum forcing [denoted by "(·)_T"] is changed from the JRA-55-based field to the CESM1 TOGA-based field for each perturbation experiment. For example, TOGA_H+JRA_T+JRA_B uses the anomalous diabatic heating calculated from CESM1 TOGA (i.e., the "TOGA_H" component), while the basic state and transient momentum forcing are still taken from JRA-55 (i.e., the "JRA_T+JRA_B" component). As a result, by differing the stationary wave responses simulated by TOGA_H+JRA_T+JRA_B (see Figs. S1a,d in the online supplemental material) and JRA_all (Figs. 2a,d), the contribution from the difference in diabatic heating can be isolated as shown in Figs. 3a and 3d. In a similar way, the contribution from anomalous transient momentum forcing bias can be extracted by comparing JRA_H+TOGA_T+JRA_B (Figs. S1b,e) and JRA_all as given in Figs. 3b and 3e. Similarly, the role played by the difference in the basic state can be derived by comparing JRA_H+JRA_T+TOGA_B (Figs. S1c,f) and JRA_all as shown in Figs. 3c and 3f.

It is clear that the bias field (i.e., Figs. 1c,f; see also Figs. 2c,f) is mostly explained by the difference in the modeled and simulated diabatic heating anomalies (Figs. 3a,d). To be specific, TOGA_H+JRA_T+JRA_B is accompanied by an overly
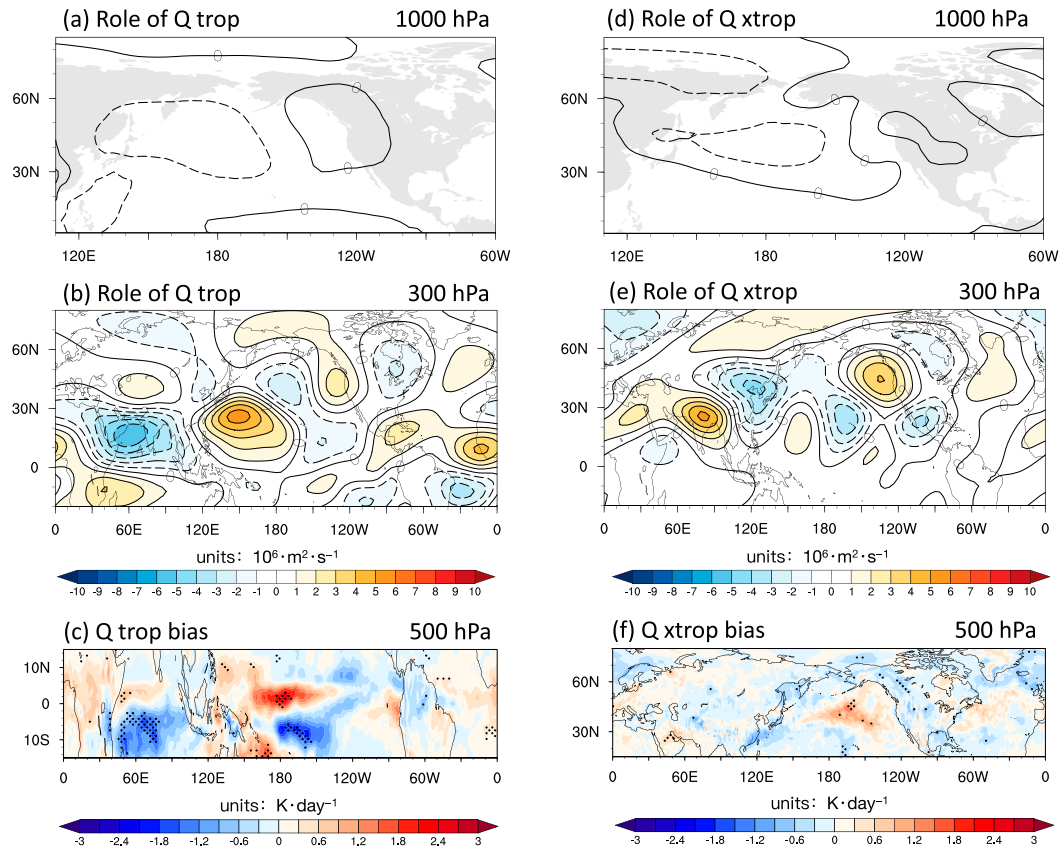
FIG. 4. Stationary wave components of the 1000- and 300-hPa streamfunction anomalies simulated by (a),(b) the difference between TOGA_trop and JRA_trop experiments in Table 2 for isolating the role of tropical diabatic heating and (d),(e) the difference between TOGA_xtrop and JRA_xtrop experiments for isolating the role of extratropical diabatic heating. (c),(f) The 500-hPa diabatic heating bias in TOGA composited over the tropical (15°S–15°N) and extratropical (15°–80°N) region respectively.

strong lower-level North Pacific cyclonic response compared to JRA_all (Fig. S1a and Fig. 3a), which is very similar to the stationary wave response simulated by the TOGA_all experiment (Figs. 2b,c). By contrast, the response caused by the difference in transient momentum (Fig. 3b) or basic state (Fig. 3c) is much weaker. At the upper level, the biased wave train structure (Figs. 1f and 2f) is most clearly seen in Fig. 3d, as a stronger wave propagating from the equatorial central Pacific to the mid- to high latitudes of the North Pacific and North America. At the lower level, no evident biased stationary wave propagation pattern can be detected when only the contribution from transient momentum forcing (Fig. 3e) or basic state (Fig. 3f) is considered in the SW model.

Note that the distinct quadrupole pattern as shown by Figs. 1f and 2f is inadequately simulated by Fig. 3d, which can be explained by the lack of interaction with transient forcing (Fig. S2). It is well known that there is a two-way interaction between transient eddy activities and the large-scale wave patterns, but the SW model is incapable of simulating this. Therefore, whether the contribution from transient momentum forcing shown by the SW model is a feedback onto the stationary wave anomalies produced by the heating bias is unclear from the stationary wave

model alone. We will use a series of comprehensive GCM simulations to further validate the findings given by the SW model. At this point, we can conclude that the diabatic heating bias is the dominant factor leading to the biased circulation in TOGA. As shown in Figs. 4c and 4f, significant diabatic heating biases can be detected over both the tropical and extratropical regions. Therefore, the next step is to isolate the key biased heating region with the aid of the SW modeling method.

c. Isolating the key biased heating region

To explore the relative importance of the tropical (15°S–15°N; Fig. 4c) and extratropical (15°–80°N; Fig. 4f) diabatic heating biases, four heating perturbation experiments are carried out as summarized in Table 2. As the role played by the transient momentum forcing is trivial compared to diabatic heating, in this section the contribution from transient momentum forcing is not considered. For the basic state, all the experiments are based on the CESM1 TOGA simulations, but the modeling results do not change qualitatively if the basic state is taken from JRA-55. The modeling results for the tropical heating-only ("JRA_trop" and "TOGA_trop") and extratropical heating-only ("JRA_xtrop" and "TOGA_xtrop") experiments

TABLE 2. Stationary wave modeling configurations for isolating the key biased heating region. Basic state is the FM climatology of winds and temperature during 1958–2010 from the CESM1 TOGA simulations. Diabatic heating anomalies are composited during FM of the El Niño years.

Experiment	Heating
JRA_trop	JRA (15°S–15°N)
TOGA_trop	TOGA (15°S–15°N)
JRA_xtrop	JRA (15°–80°N)
TOGA_xtrop	TOGA (15°–80°N)
TOGA_IO	TOGA (15°S–15°N, 40°–110°E)
JRA_IO	JRA (15°S–15°N, 40°–110°E)
TOGA_WP	TOGA (15°S–15°N, 110°E–180°)
JRA_WP	JRA (15°S–15°N, 110°E–180°)
TOGA_CP	TOGA (15°S–15°N, 180°–110°W)
JRA_CP	JRA (15°S–15°N, 180°–110°W)

are given in Figs. S3 and S4, respectively. Their relative contribution for the North Pacific circulation bias can be more directly seen using Fig. 4. It is striking that the upper-level wave propagation features simulated by the "trop" experiments (Fig. 4b) are very close to the bias field derived directly from JRA-55 and TOGA simulations (Fig. 1f). Compared to Fig. 2, the north Indian Ocean–Asian region is even better simulated in the tropical heating-only configuration, suggesting that unrealistic tropical–extratropical interaction and transient feedback in the SW model is likely the main reason for the limited model accuracy over this region. The extratropical diabatic heating difference also contributes to the enhancement of the circulation bias at the lower level near the surface (Fig. 4d). In the

upper layer, although a strong anticyclonic response to extratropical diabatic heating can be seen over the west coast of North America, no significant bias signal can be detected to its west over the North Pacific region (Fig. 4e).

Recall that in our calculation the diabatic heating is derived from Eq. (1) using monthly data, so that the heat transport by transients is included. We can remove the contribution from transients by recalculating the observed diabatic heating from Eq. (1) at a higher frequency (6 hourly). For the TOGA simulation, the diabatic heating without contribution from transient heat transport is available as the sum of the shortwave heating rate (QRS), longwave heating rate (QRL), temperature tendency due to moist process (DTCOND), and vertical diffusion (DTV) in the model output variables. After removing the contribution from transients, the signal caused by extratropical heating is greatly reduced (not shown). Therefore, the extratropical feedback shown here is mainly associated with the transient eddy heat flux convergence.

The structure of the springtime tropical diabatic heating bias is given in Fig. 5b. Significant bias signals can be detected over three major ocean basins: a negative bias over the tropical Indian Ocean (IO; 15°S–15°N, 40°–110°E), a positive bias over the tropical central-western Pacific (WP; 15°S–25°N, 110°E–180°), and a negative bias over the tropical central Pacific (CP; 15°S–15°N, 180°–110°W). According to Fig. S5, the negative diabatic heating bias over the IO is caused by the extra anomalous cooling simulated by TOGA but not present in the reanalyses. The positive bias signal over the WP can be explained by the fact that the TOGA simulated diabatic cooling anomalies are too weak compared to that in JRA-55. The bias distribution over the CP consists of an antisymmetric
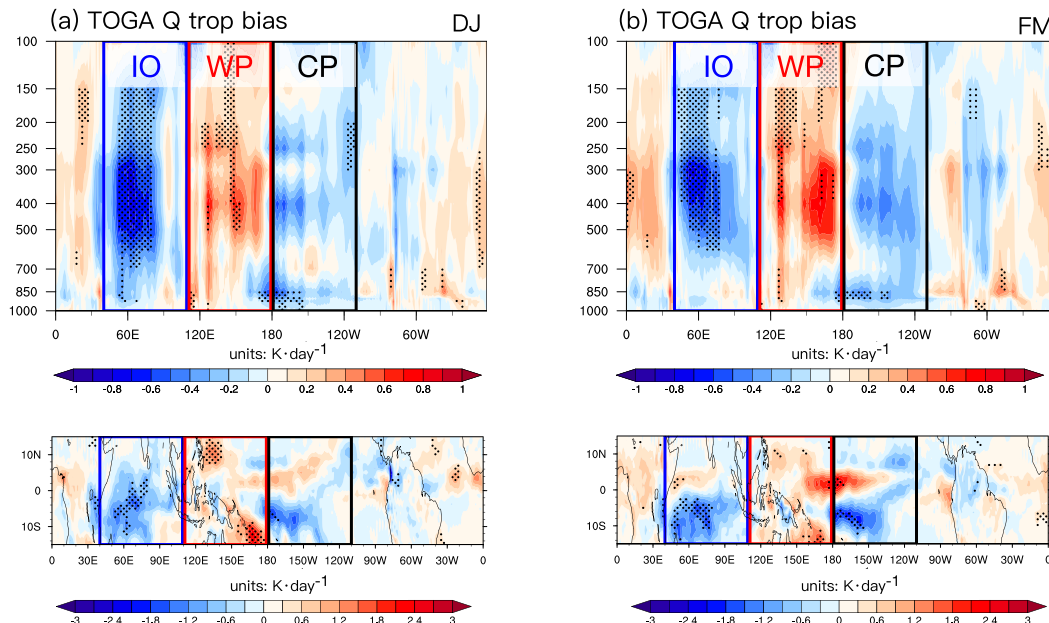

FIG. 5. (a) DJ and (b) FM-averaged tropical diabatic heating bias in CESM1 TOGA simulations during FM of El Niño events from 1958 to 2010. (top) The vertical cross section averaged over 15°S–15°N. (bottom) The horizontal distribution at 500 hPa. The area that exceeds significance at the 95% confidence level is stippled.
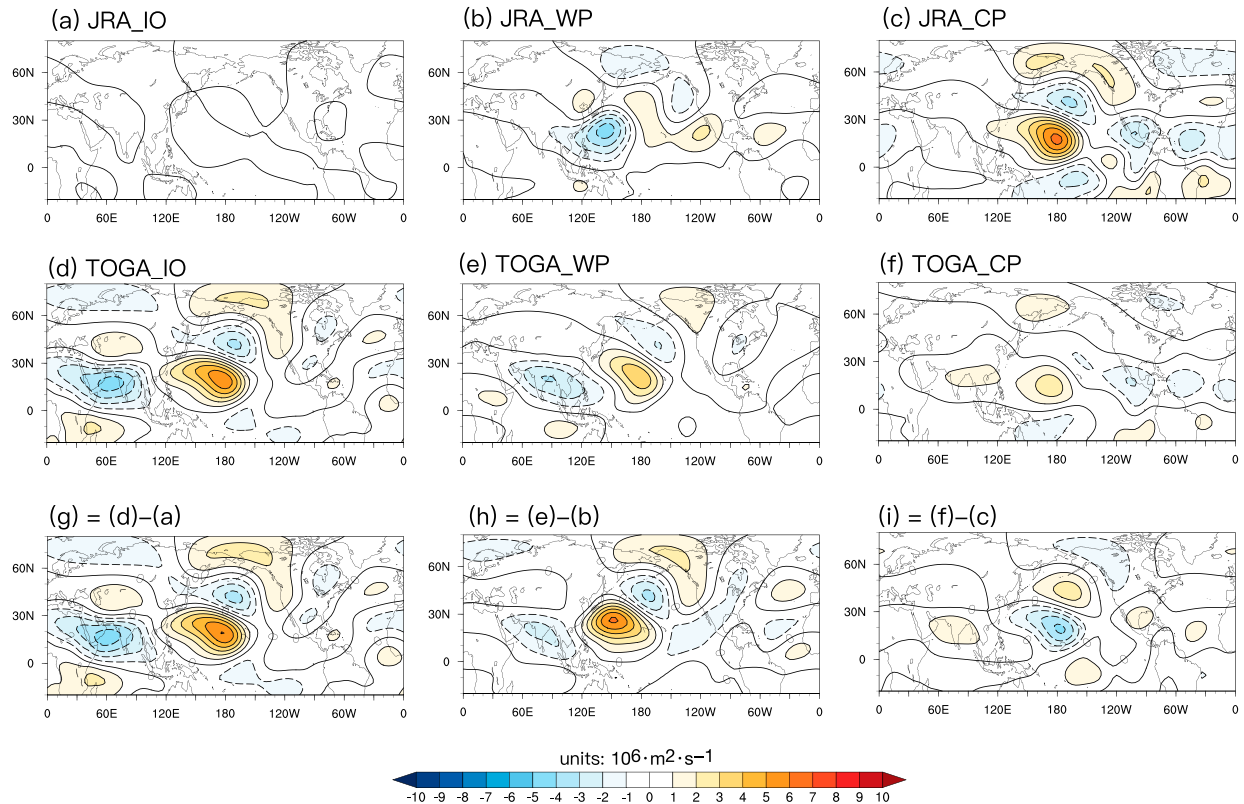
FIG. 6. Stationary wave components of the 300-hPa streamfunction anomalies simulated by the single-basin diabatic heating forcing experiments in Table 2 with input fields based on (a)–(c) JRA-55 reanalyses and (d)–(f) CESM1 TOGA simulations, and (g)–(i) their differences, forced by (left) IO heating only, (center) WP heating only, and (right) CP heating only.

structure about the equator (i.e., positive to the north but negative to the south). As can be seen from Fig. S5, this antisymmetric structure can be explained by the overly strong and limited southward extension of the heating field in CESM1 TOGA. A similar bias structure can be consistently detected based on different reanalyses data [NCEP–NCAR (R1), ERA20C, ERA-Interim (ERAI), ERA5, and CFSR] as shown in Fig. S6.

We can further assess the role played by the diabatic heating bias in each tropical basin by imposing the IO, WP, or CP diabatic heating exclusively in the SW model (Table 2). The modeling results indicate that the diabatic heating differences over the IO and WP positively contribute to the cyclonic circulation bias over the North Pacific (Figs. 6g,h). Specifically, the extra cooling effects over the IO in TOGA cause a wave train response with anticyclonic anomalies over the tropical western Pacific and cyclonic anomalies over the North Pacific. As no obvious IO heating anomalies are seen in JRA-55 (Fig. S5), its wave response is accordingly much weaker in Fig. 6a. As a result, the contribution revealed by Fig. 6g is mostly a manifestation of the IO cooling effects in TOGA. For the WP, the modeled wave train response forced by the TOGA-based heating anomalies (Fig. 6e) is similar to that forced by the IO (Fig. 6d) but with a weaker amplitude. The insensitivity of the stationary wave response to the location of

the tropical heating source has been found by many previous studies (Simmons et al. 1983; Branstator 1985; Ting and Yu 1998). When forced by the WP diabatic heating anomalies based on JRA-55 (Fig. 6b), significant circulation anomalies can be found as a cyclonic system located to the east of the Philippines. The eastern part of the North Pacific is associated with anticyclonic anomalies while its western part displays a cyclonic response. When looking at the JRA_CP and TOGA_ CP experiments, the stationary wave response modeled by TOGA CP heating (Fig. 6f) is weaker than that modeled by JRA-55 (Fig. 6c). As a result, the circulation anomalies caused by their heating difference consist of an anticyclone response over the North Pacific region (Fig. 6i), which opposes the biased circulation as a whole. As can be seen from Fig. 4c, the diabatic heating bias over the CP is of opposite sign in the north and south of the equator. To investigate the relative influence of these two regions, two more simulations are carried out by specifying the northern and southern parts of the CP heating bias into the SW model separately. The result indicates that the North Pacific anticyclonic anomalies shown in by Fig. 6i are mostly due to the lack of southern warming effects (i.e., cooling bias) in TOGA (Fig. S7). In summary, during the springtime (FM) after the peak of El Niño events, the diabatic heating bias over the IO and WP jointly lead to the overestimation of the North Pacific cyclonic circulation

TABLE 3. Stationary wave modeling configurations for understanding seasonality of the teleconnection bias. The basic state is the DJ/FM climatology of winds and temperature during 1958–2010. Diabatic heating forcing is the difference between TOGA and JRA-55 composited anomalies (i.e., diabatic heating bias in TOGA) during DJ/FM of the El Niño years.

Experiment	Basic state	Heating
FM_H+FM_B	TOGA FM	FM (TOGA-JRA)
DJ_H+FM_B	TOGA FM	DJ (TOGA-JRA)
FM_H+DJ_B	TOGA DJ	FM (TOGA-JRA)

response in the model. The weak cooling bias over the CP, when the tropical diabatic heating anomalies during ENSO force the extratropical teleconnection, partially offsets the role played by the IO and WP heating bias.

d. Understanding the seasonality of the teleconnection bias

Chen et al. (2020) demonstrated that the overly strong North Pacific ENSO teleconnection bias appears during the springtime (FM) and is not present during the peak ENSO months [December–January (DJ)]. What causes this seasonality in the bias? Based on the above analyses, a reasonable speculation would be the differences in the tropical diabatic heating bias. However, the tropical diabatic heating bias

averaged over the previous winter months (Fig. 5a) suggests that a significant heating bias has already built up in winter and the distribution of the bias signal during DJ is very similar to that during FM, as a negative–positive–negative structure spanning the IO, WP, and CP basins, respectively. However, its amplitude over the WP (IO) during DJ is weaker (stronger) than that during FM.

To investigate why the bias appears in FM and not DJ, three additional experiments are carried out using the SW model. Considering the fact the nonlinear effects between the diabatic heating and basic state are weak, instead of carrying out two independent simulations as "JRA_trop" and "TOGA_trop", the tropical diabatic heating biases are first calculated and put into the SW model directly in this section (Table 3). The modeling results suggest that only minor differences can be detected between these two approaches (cf. Figs. 4a,b and 7a,b). By sticking to the FM basic state ("FM_B") and combining it with the diabatic heating biases during FM or DJ ("FM_H" or "DJ_H"), we find that the modeled stationary wave response to the DJ-averaged tropical heating bias is even stronger than that to the FM heating bias (cf. Figs. 7a,b or 7d,e). Thus, the difference in the DJ and FM diabatic heating bias is not the main reason for the seasonality of the bias occurrence. However, if the FM diabatic heating bias is added to the DJ-averaged basic state in the SW model ("FM_H+DJ_B"), it is obvious that the wave response
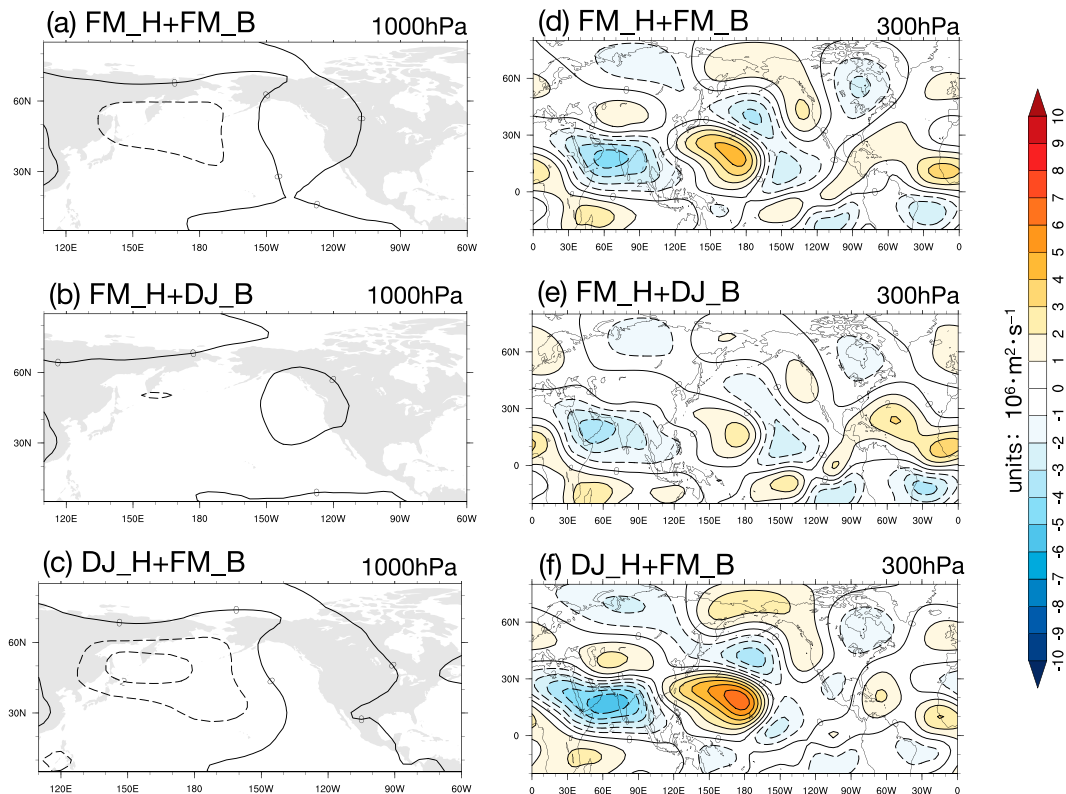

FIG. 7. Stationary wave components of the (left) 1000- and (right) 300-hPa streamfunction anomalies simulated by the (a),(d) FM_H+FM_B, (b),(e) FM_H+DJ_B and (c),(f) DJ_H+FM_B experiments for understanding seasonality of the teleconnection bias in Table 3.
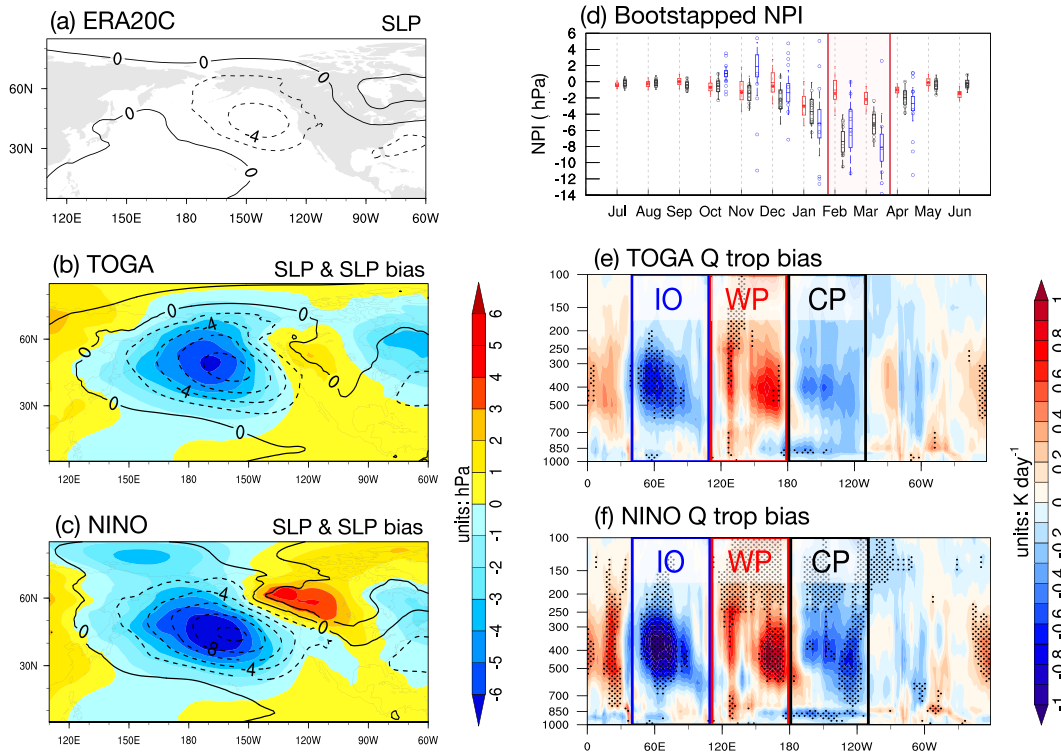
FIG. 8. FM-averaged SLP anomalies (contour lines) during El Niño events for (a) ERA20C and (b) CESM1 TOGA simulations, and (c) the difference between EN and CTRL (i.e., NINO) experiments in CAM5. Shading in (b) and (c) is the bias fields compared to ERA20C. (d) Seasonal evolution of the bootstrapped NPI (hPa) calculated from ERA20C (red), CESM1 TOGA simulations (black), and CAM5 NINO experiments (blue). The box height indicates the 25%–75% confidence interval of the NPI composites. See Chen et al. (2020) for more details. Also shown are FM-averaged tropical (15°S–15°N) diabatic heating bias during El Niño events for (e) CESM1 TOGA simulations and (f) CAM5 NINO experiments. Regions that exceed the 95% confidence level of significance are stippled.

is weakened considerably (cf. Figs. 7a,b or 7d,e). Therefore, the springtime basic state is conducive to a larger amplitude stationary wave response than the winter basic state even when forced by the same diabatic heating anomalies. In other words, the seasonal evolution of the background state, rather than the difference in the diabatic heating field between DJ and FM, leads to the ENSO teleconnection bias occurring preferentially in spring. The question then becomes: Why is the springtime basic state conducive to a larger-amplitude stationary wave response than winter? Possible answers to this question will be provided in the discussion section of this paper.

4. Bias correction in CAM5

The SW model is useful for diagnosing the relative contributions from different factors driving the stationary wave response. However, it is highly simplified compared to a comprehensive GCM. As found using the SW model, the transient feedback over the extratropical region appears to play a role in enhancing the bias circulation. However, the anomalous transient eddy activities may have a tropical origin in a comprehensive GCM, where the transients are able to respond to the tropical forcing. To test the hypothesis that the full circulation bias has an ultimate origin in the tropics, a

series of bias-correction experiments are carried out in this section. The model used is CAM5, which is the same as the one used in the CESM1 TOGA simulation. The El Niño response is determined using the NINO simulations (see section 2 for details).

The ensemble mean of the North Pacific anomalies in CAM5 NINO are compared to the ERA20C, and the CESM1 TOGA simulations in Figs. 8a–c. The overly strong negative SLP anomalies over the North Pacific seen in the TOGA experiments are reproduced by the NINO experiments. Following Chen et al. (2020), the North Pacific Index (NPI) is calculated using area-averaged SLP anomalies over 35°–60°N, 165°E–145°W. Figure 8d displays the seasonal evolution of the NPI in observations, TOGA simulations, and NINO experiments. The uncertainties induced by the sampling error are estimated by bootstrapping (Deser et al. 2017, 2018; Chen et al. 2020). By resampling the ENSO events with replacement repeatedly, the bootstrapping technique aims to form synthetic ENSO composites to characterize the uncertainties caused by sampling fluctuation arising from internal variability. For TOGA and NINO, the NPI bias is most significant from February to March. In the TOGA simulations, the lowest value of NPI (i.e., the largest amplitude) occurs in February, which is one month delayed compared to
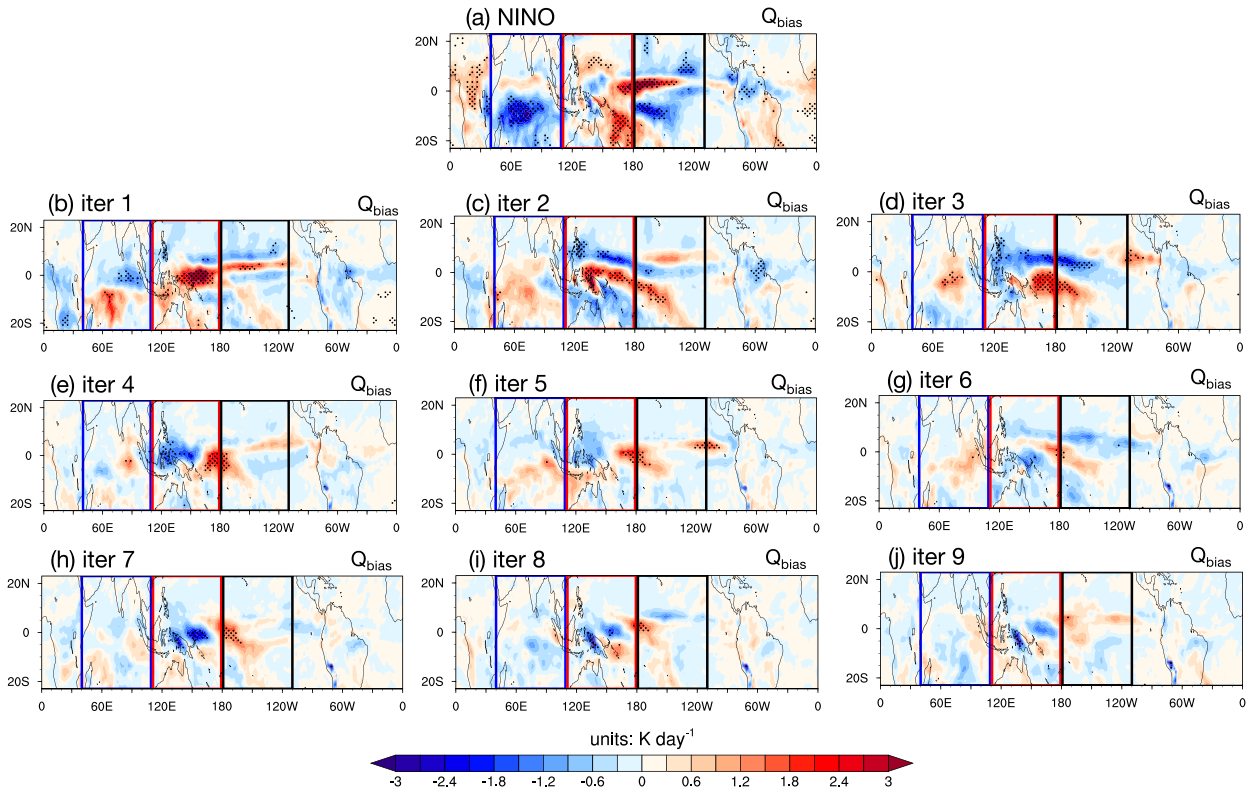
FIG. 9. Evolution of the 500-hPa tropical diabatic heating bias by applying the iterative bias-correction technique in CAM5.

observations. In the NINO experiments, the NPI amplitude peaks one month even later in March. Therefore, by forcing the model with a canonical El Niño SST pattern and comparing to a simulation with prescribed climatological SSTs, the major characteristics of the springtime North Pacific ENSO teleconnection bias that was found in CESM1 TOGA can be largely reproduced. The stronger circulation bias in the NINO experiment compared to TOGA is in agreement with its stronger tropical diabatic heating bias seen over the tropical Indian Ocean (IO) and central-western Pacific (WP; cf. Figs. 8e and 8f). We will now use this setup to correct the ENSO-induced diabatic heating biases in the comprehensive GCM and demonstrate that the tropical heating biases are the ultimate driver of the extratropical teleconnection bias.

a. Iterative bias-correction approach

To artificially "correct" the tropical diabatic heating in NINO, we add a bias-correction term to the EN experiments' thermodynamic equation as a modification of the temperature tendency produced at the end of the physics time step (i.e., every 30 min). This bias correction tendency is calculated for each month (October to April) and imposed over the tropical band within 23°S–23°N, which is a little wider than the region considered by the SW model in previous sections. We cannot simply impose the heating bias multiplied by −1 in the model, because the model would nonlinearly amplify the modification effects due to feedback mechanisms. This "overreacting consequence" inhibits us from ideally correcting the bias field

in one step. The solution proposed is by adopting an "iterative approach," which consists of two key steps: 1) a scaling factor is adopted to scale down the correction term to partially offset the amplification effects caused by positive feedbacks in the model and 2) the initial guess of the bias-correction term is optimized iteratively according to the residual bias in each iteration step. The bias-correction term used in each step is estimated by

$$Q_{\text{crct}}^{(i)} = \begin{cases} -1 \times (Q_{\text{bias}}^{\text{NINO}} \times 0.25), & \text{when } i = 1 \\ Q_{\text{crct}}^{(i)} = Q_{\text{crct}}^{(i-1)} - Q_{\text{bias}}^{(i-1)} \times 0.25, & \text{when } 2 \le i \le 6, \\ Q_{\text{crct}}^{(i)} = Q_{\text{crct}}^{(i-1)} - Q_{\text{bias}}^{(i-1)} \times 0.1, & \text{when } 7 \le i \le 9 \end{cases} \quad (2)$$

where $Q_{\text{crct}}^{(i)}$ is the bias correction term for modifying the temperature tendency in the "iter i" experiment, where i is the iteration step. The scaling factor is set to 0.25 from step 1 to step 6, and changed to 0.1 from step 7 to step 9 as the residual bias becomes smaller. The term $Q_{\text{bias}}^{\text{NINO}}$ is the initial tropical heating bias in the NINO experiment, and $Q_{\text{bias}}^{(i-1)}$ is the residual bias after applying $(i - 1)$ steps of corrections. The specific definition for Q_{bias} in each step is

$$Q_{\text{bias}}^{\text{NINO}} = (Q_{\text{EN}} - Q_{\text{CTRL}}) - Q_{\text{obs}}$$
$$Q_{\text{bias}}^{(i)} = (Q_{\text{iter}}^{(i)} - Q_{\text{CTRL}}) - Q_{\text{obs}} \quad (3)$$

where Q_{obs} is the tropical diabatic heating anomalies during the El Niño events based on JRA-55 reanalyses. The tropical
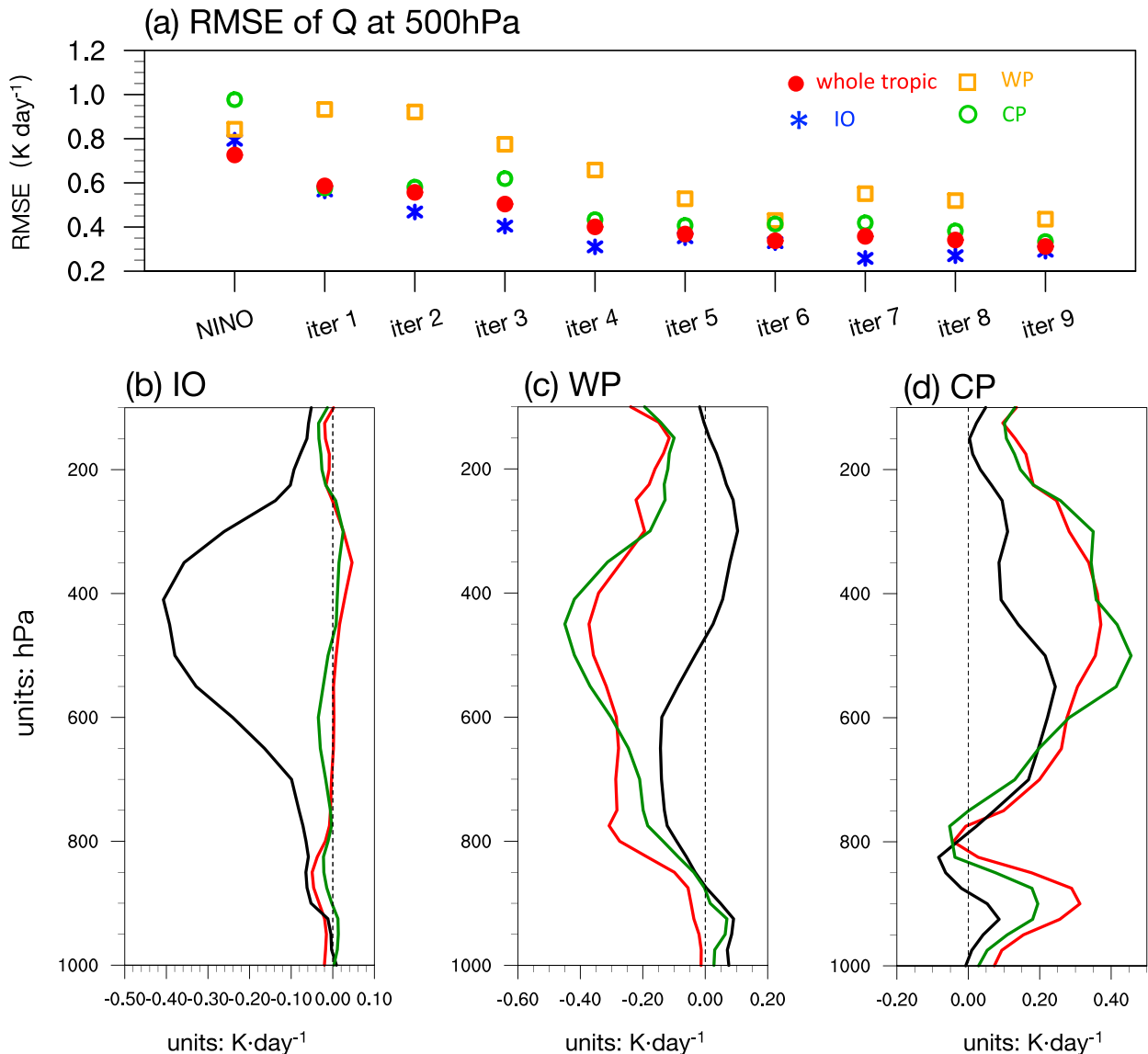
FIG. 10. (a) The root-mean-square error (RMSE) of the diabatic heating fields at 500 hPa in each iteration step for the whole tropical band (red dots), the tropical Indian Ocean (IO; 23°S–23°N, 40°–110°E; blue stars), the tropical central-western Pacific (WP; 3°S–23°N, 110°E–180°; orange squares), and the tropical central Pacific (CP; 23°S–23°N, 180°–110°W; green circles) respectively. (b)–(d) Comparison of the heating profile for each basin before and after applying the bias-correction technique. Red is for the observation based on JRA-55, black is for CAM5 experiments before bias correction (EN minus CTRL), and green is for the CAM5 experiments after 9 steps of iterative bias-correction (iter 9 minus CTRL).

diabatic heating fields in the CTRL, EN, and iter i experiments are denoted as Q_{CTRL}, Q_{EN}, and $Q_{iter}^{(i)}$ respectively. For $Q_{iter}^{(i)}$, it is the sum of the model generated heating and the $Q_{crct}^{(i)}$ term added into the model.

b. Effectiveness of the bias-correction approach

To illustrate the effectiveness of the iterative bias-correction approach, the 500-hPa tropical diabatic heating bias (Q_{bias}) at each iteration step is given in Fig. 9. Generally, the amplitude of the bias becomes smaller as the iteration step increases. Most of the significant heating bias has been wiped out after nine steps of iterative correction, except for the extra cooling signals remaining over western New Guinea (Fig. 9i). The improvements can be more quantitatively evaluated by calculating the root-mean-square error (RMSE) in each iteration step as shown in Fig. 10a. For the tropical region as a whole, the RMSE value displays a monotonically decreasing trend with a slight increase seen in iter 7 (the seventh iteration) due to the increase of the bias signal over WP and CP. The trend in RMSE for each single ocean basin is less monotonic. The ultimate goal of conducting the iterative
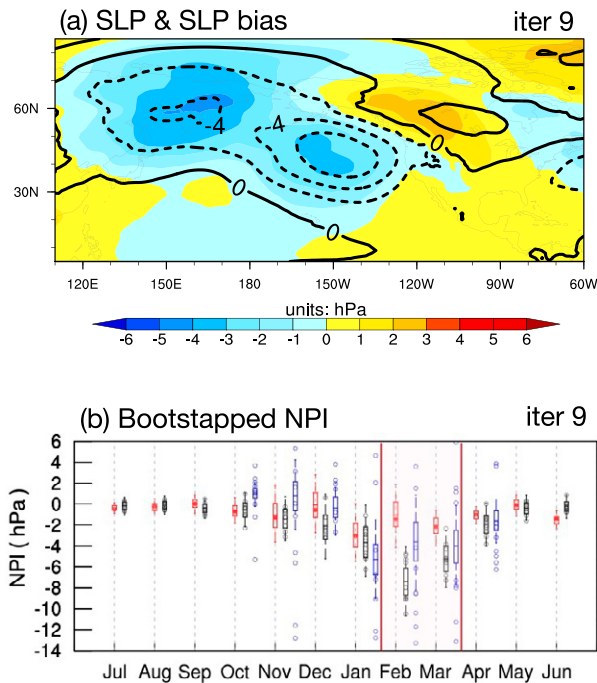
FIG. 11. FM-averaged SLP simulated by (a) the difference between iter 9 and CTRL experiments (contour lines) and the bias of this difference with respect to observations (ERA20C; color shading). (b) Seasonal evolution of the bootstrapped NPI (hPa) calculated from ERA20C (red) and CESM1 TOGA simulations (black), and the difference between iter 9 and CTRL experiments (blue). The box height indicates the 25%–75% confidence interval of the NPI composites. See Chen et al. (2020) for more details.

bias-correction approach is to obtain one simulation whose tropical diabatic heating bias is largely eliminated, and we consider this to have been achieved by iter 9. Significant improvement can be detected at all vertical levels, especially in the middle and upper troposphere where the original bias is most evident (Fig. 10; see also Fig. S8). Continuing this iterative process further does not produce substantial improvements (not shown). Therefore, the iter 9 experiment is taken as the one that meets the expectation of a successful bias-correction outcome in CAM5.

c. Improvement in circulation response

To look at the corresponding change in the circulation response, the anomalies are composited as the difference between the ensemble mean of the iter 9 and CTRL simulations in Fig. 11a. Also given is the bootstrapped NPI evolution in Fig. 11b. After "correcting" the tropical diabatic heating, the simulated North Pacific circulation response is significantly weakened, although it still overestimates the amplitude compared to ERA20C (color shading in Fig. 11a). In addition, the anomaly center is located farther eastward in the iter 9 experiment, so that the westward shifting bias is erased as well. The improvement is also seen in the seasonal evolution features. For the CESM1 TOGA simulation and the CAM5 NINO simulations, the peak time of the NPI

amplitude is delayed compared to that in observations. In the iter 9 experiment, the NPI peaks in January, the same month as observations. The residual bias in the heating field reveals that there are weak positive biases over the CP (Fig. 9i). Taking the residual heating bias in the iter 9 as the anomalous forcing in the SW model, we find that the weak heating bias over the CP is the main cause of the residual North Pacific cyclonic circulation bias seen in iter 9 (see Fig. S9).

The upper-level anomalous circulation as depicted by the 300-hPa streamfunction and 150-hPa velocity potential is shown in Fig. 12 for observations, NINO and iter 9. In NINO, the upper-level circulation bias is manifested as a convergence center over the tropical Indian Ocean (Fig. 12h). In observations, the anomalous convergence center is located over the Maritime Continent with another divergent center to the east (Fig. 12g). The strong tropical Indian Ocean convergence bias can be explained by the diabatic cooling bias over the IO, which would induce sinking motion and upper-level convergence. For the anomalous upper-level streamfunction field, a cyclonic bias can be seen to the northwest of the Arabian Peninsula in NINO (Fig. 12e), which is also linked to the IO diabatic cooling bias by a geostrophic adjustment mechanism to the sinking motion. The observed streamfunction anomalies feature a negative–positive–negative wave structure around 140°–150°E, propagating from the tropics to the middle and high latitudes of the North Pacific (Fig. 12d). A similar tripole pattern can also be detected in the NINO experiment but with a westward shift and an intensification of the northernmost cyclonic anomalies. After "removing" the tropical diabatic heating bias, the dipole structure in the anomalous potential velocity field and the tripole structure in the anomalous streamfunction field are approaching the observations as shown in Figs. 12i and 12f. At 1000 hPa (Figs. 12a–c), the cyclonic anomalies over the North Pacific region are weakened accordingly in iter 9 compared to NINO, but still stronger than that in observations, consistent with the SLP fields shown in Fig. 11a. The improvement upon bias correction can be reasonably traced back to the wave dynamics at upper levels which is directly linked to the improvements in the tropical forcing (Figs. 9 and 10). Furthermore, it is also proven by the iter 9 experiment that the extratropical feedback is tied to the tropical diabatic heating bias, as the extratropical heating bias is much weakened after alleviating the tropical bias (see Fig. S10). In conclusion, the bias-correction experiment carried out in CAM5 further proves that the springtime North Pacific ENSO teleconnection bias in CESM1 is of tropical origin.

5. Summary and discussion

The North Pacific ENSO teleconnection communicates the influence of tropical SST anomalies to the higher latitudes of the Northern Hemisphere. Although the ENSO-related SST anomalies and the induced North Pacific circulation response usually peak during the winter season, previous studies have attributed some extreme events happening during spring to the prolonged effects of ENSO (Jong et al. 2016; Wolter et al. 1999; Schmidt et al. 2001; Cook et al. 2017). There is also evidence
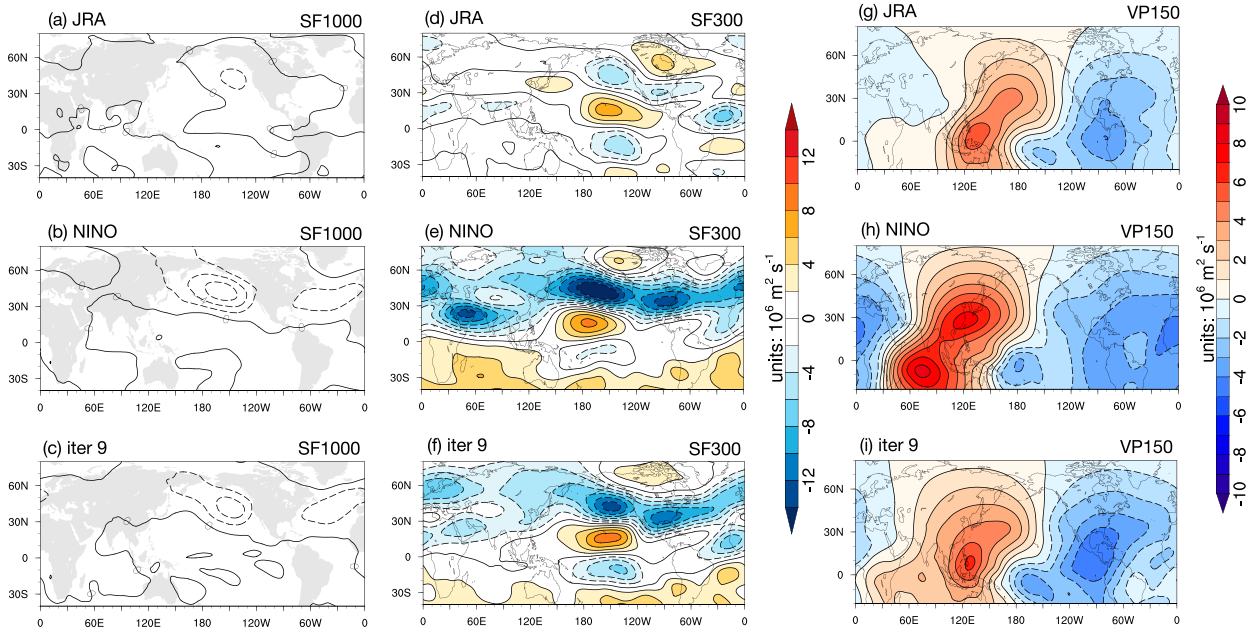
FIG. 12. FM-averaged streamfunctions at 1000 hPa for (a) JRA-55's El Niño years' composite anomalies, (b) the difference between EN and CTRL experiments, and (c) the difference between the iter 9 and CTRL experiments. (d)–(f) As in (a)–(c), but for streamfunctions at 300 hPa. (g)–(i) As in (a)–(c), but for velocity potential at 150 hPa.

showing that the potential predictability for the ENSO climate influence is even higher in spring (Kumar and Hoerling 1998). Therefore, an accurate simulation of the springtime North Pacific ENSO teleconnection by climate models is of great importance for the attribution and forecasting of springtime anomalous events related to ENSO. However, the modeled springtime North Pacific ENSO teleconnection is overly strong compared to observations (Alexander et al. 2002; Spencer and Slingo 2003; Chen et al. 2020). Here, we have investigated the origins of this bias.

With the aid of the stationary wave (SW) model, the relative contributions from the basic state, the anomalous diabatic heating, and the anomalous transient forcing are disentangled. It is found that the deficiency in the simulated tropical Indian Ocean (IO) and tropical central-western Pacific (WP) diabatic heating anomalies is the main cause of the springtime North Pacific cyclonic bias during the El Niño events in CESM1 TOGA simulations. In contrast, the central Pacific (CP) diabatic heating bias counteracts that produced by the other two regions.

Although the difference between the modeled and observed basic state does not give rise to the bias occurrence directly, the natural seasonal evolution of the basic state in both observations and CAM dictates the seasonality of the bias. This is because the springtime basic state favors a stronger stationary wave response to the tropical diabatic heating anomalies associated with ENSO than the wintertime basic state, as elucidated in our SW modeling experiments.

The role of transient eddies is composed of two parts: 1) Transient heat transport could locally reinforce the lower-level bias circulation. Specifically, the transient eddy heat flux convergence is essential in forming the extratropical

heating bias seen in Fig. 4f, which contributes to the enhancement of the North Pacific circulation bias shown in Fig. 4d. 2) Transient vorticity flux is essential for modulating the wave response structure, as the biased North Pacific quadrupole pattern is better simulated after including the transient momentum forcing (cf. Fig. S2 and Fig. 3). However, the SW model is incapable of simulating the two-way interactions between transient eddy activities and the large-scale wave structure. Through comprehensive GCM simulations, it is further shown that the transient eddy activities are inseparable from the large-scale wave response triggered by the tropical diabatic heating anomalies. Therefore, the role played by the transients is considered to be secondary.

To verify the conclusions drawn from the SW model, additional experiments are carried out with a full general circulation model (CAM5). An iterative bias-correction approach is adopted to modify the CAM5 diabatic heating response to observed El Niño events such that the ultimate diabatic heating field resembles observations. This approach is shown to effectively eliminate the tropical diabatic heating bias over all the three ocean basins (i.e., the IO, the WP, and the CP). In response to the "improved" tropical heating forcing field, the North Pacific circulation response is significantly improved: its intensity, center location, and seasonal evolution are all much closer to the observations, further indicating that the springtime North Pacific ENSO teleconnection bias is tied to the tropical diabatic heating bias in the model.

Our findings raise a number of additional questions:

1) Are the bias formation mechanisms for the La Niña events equal and opposite to those for El Niño? To
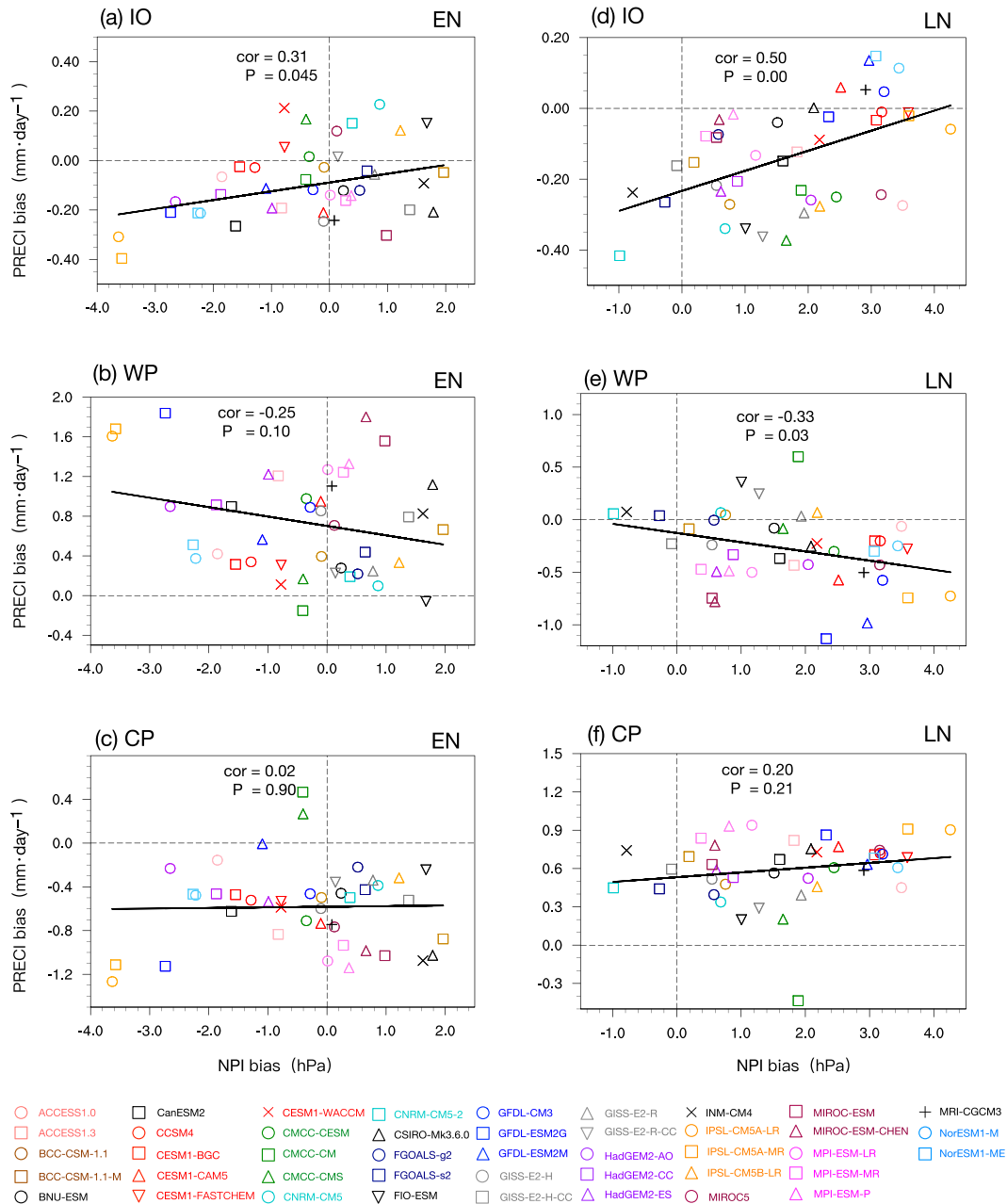
FIG. 13. Scatterplots of the relationship between the tropical precipitation biases and the NPI biases across CMIP5 models during FM of (left) El Niño and (right) La Niña composite events. The precipitation biases are area averaged for the (a),(d) IO, (b),(e) WP, and (c),(f) CP.

answer this question, the tropical diabatic heating bias during La Niña events are composited in TOGA and shown in Fig. S11. It is clear that the tropical diabatic heating bias over the three ocean basins has a similar pattern to that during El Niño but with opposite sign, i.e., the IO and the CP are associated with positive heating bias, while the WP displays an overly strong cooling effect. When the biased heating fields for composite La Niña events are imposed in the SW model (Table S1), the results suggest that the positive diabatic heating bias over the IO and the negative bias over the WP positively contribute to the formation of the North Pacific anticyclonic bias during La Niña events (Fig. S12). In contrast, the diabatic heating bias over the CP has an opposite effect by leading to a weak cyclonic response. It is concluded that the bias formation mechanism behind La Niña events can be roughly viewed as equal and opposite to that during El Niño.
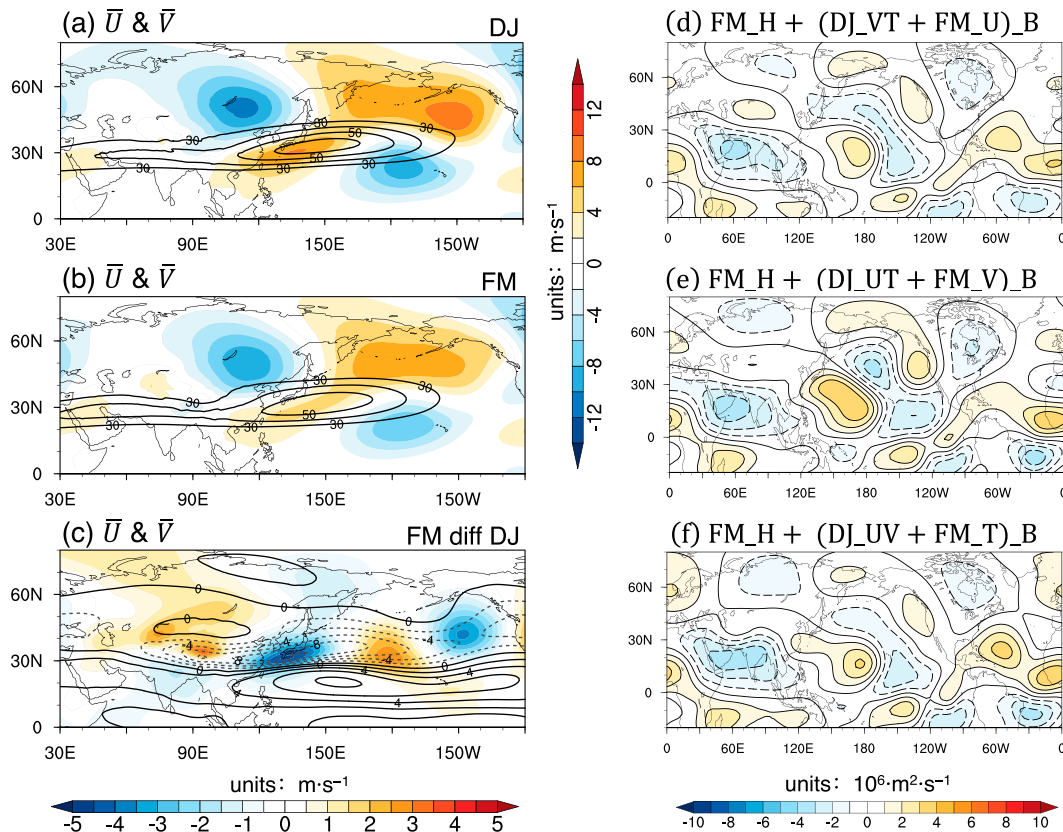
FIG. 14. (left) Climatological zonal (contour lines) and meridional (color shaded) winds at 300 hPa from TOGA simulations during (a) DJ and (b) FM of 1958–2010, with (c) their difference (FM minus DJ). (right) Stationary wave components of the 300-hPa streamfunction anomalies simulated by the (d) "FM_H+(DJ_VT+FM_U)_B", (e) "FM_H+(DJ_UT+FM_V)_B", and (f) "FM_H+(DJ_UV+FM_T)_B" experiments in Table 4.

2) Is there evidence for similar origins of the bias in other models? According to Fig. 6 of Chen et al. (2020), the North Pacific ENSO teleconnection bias can be detected in most CMIP5 models. As a preliminary investigation into the universality of the cause of bias in these different models, a scatterplot of the relationship between the tropical precipitation bias and the NPI bias across 43 CMIP5 models [Table 1 of Chen et al. (2020)] is plotted in Fig. 13. A significant correlation is found between both the IO (positive correlation) and WP (negative correlation) precipitation bias and the NPI bias for both El Niño and La Niña in spring (FM). However, no significant correlation is found between the CP precipitation and NPI biases. This suggests that the bias formation mechanism revealed in CESM1 TOGA simulations may also exist in other models. For further model development aiming at improving the springtime ENSO teleconnections, it is suggested that efforts should be made to optimize the precipitation simulation across different tropical ocean basins simultaneously.

3) Why is the springtime basic state more sensitive to tropical anomalous diabatic heating anomalies compared to the wintertime basic state? According to the stationary wave modeling results in section 3, the springtime basic state is

more favorable for wave propagation into the North Pacific than the wintertime basic state, even when forced by the same diabatic heating anomalies. However, the underlying mechanism has not been addressed. One possibility is due to the seasonal change in the jet stream. Another possible mechanism is the mean seasonal change in atmospheric stratification. These two possibilities are investigated in a preliminary manner in Fig. 14 by using three additional SW modeling experiments according to Table 4. Starting from the "FM_H+FM_B" and "FM_H+DJ_B" modeling results shown in Fig. 7, the role of FM basic state is decomposed into its zonal winds [through the "FM_H+(DJ_VT+FM_U)_B" experiment], meridional winds [through the "FM_H+ (DJ_UT+FM_V)_B" experiment], and temperature [through the "FM_H+(DJ_UV+FM_T)_B" experiment] components separately. As suggested by Figs. 14d–f, the difference in the background meridional winds is crucial in determining a more sensitive response seen in the FM basic state (Fig. 7e). In particular, the Rossby wave train emanating from the western tropical Pacific and arcing over the North Pacific is approximately doubled in strength under the FM meridional wind basic state compared to the FM zonal wind or temperature basic states (cf. Fig. 14e with Figs. 14d,f). As shown in Figs. 14a–c, the subtropical jet stream during FM is significantly weakened

TABLE 4. As in Table 3, but the basic state is reconstructed as follows: meridional winds and temperature from the DJ average, and zonal winds from the FM average for FM_H+(DJ_VT+FM_U)_B; zonal winds and temperature from DJ-average, and meridional winds from FM average for FM_H+(DJ_UT+FM_V)_B; and zonal and meridional winds from DJ-average, and temperature from FM average for FM_H+(DJ_UV+FM_T)_B.

Experiment	Basic state	Heating
FM_H+(DJ_VT+FM_U)_B	DJ VT but FM U	FM (TOGA-JRA)
FM_H+(DJ_UT+FM_V)_B	DJ UT but FM V	FM (TOGA-JRA)
FM_H+(DJ_UV+FM_T)_B	DJ UV but FM T	FM (TOGA-JRA)

compared to DJ. On one hand, the zonal wind speed is reduced by $8\,\mathrm{m\,s}^{-1}$ in its core region. On the other hand, the convergent (divergent) meridional winds around the jet entrance (exit) region are weakened accordingly, suggesting the mutually coupled characteristics in the zonal and meridional components of the upper-level winds along the jet stream. Therefore, the SW modeling results here indicate that the meridional wind aspect of the climatological basic state is important in determining the seasonality of the teleconnection bias as discussed in section 3, which may be further linked to a weakened subtropical jet steam during FM compared to DJ.

Despite continued improvements in the simulation of ENSO and associated teleconnections, further understanding of the air–sea coupled system outside of the central-eastern Pacific is necessary for eliminating the springtime North Pacific ENSO teleconnection bias in the models. Great challenges may exist because the IO and WP precipitation anomalies during ENSO events can be influenced by many different factors (e.g., local air–sea feedback, remote influence via an atmospheric bridge from other tropical or extratropical regions, and thermodynamic/dynamic processes in the ocean). These myriad influences should be considered in an integrated fashion for their joint contributions to the simulation and predictability of ENSO in climate models. As pointed out by many previous studies (Lau and Nath 2003; Wu and Kirtman 2005), air–sea coupling plays a vital role in regulating the IO–WP region precipitation variability. Note that this bias can be significantly found even in the coupled configuration of the CMIP models (Chen et al. 2020), indicating that AMIP simulations do not produce the bias as a result of the lack of coupling and that if air–sea coupling issues are playing a role then it must be processes that are misrepresented in both coupled and AMIP simulations. In addition, although the difference in the modeled and observed basic state is not the determining factor leading to the springtime ENSO teleconnection bias over the North Pacific region, seasonal variation in the subtropical circulation mean state explains why the bias is most significantly seen during the springtime (FM). The results of this paper suggest that a better understanding of both the tropical forcing and its interaction with the basic state is crucial for advancing the simulation and predictability of springtime ENSO teleconnections.

REFERENCES

Adler, R. F., and Coauthors, 2003: The version-2 Global Precipitation Climatology Project (GPCP) monthly precipitation analysis (1979–present). *J. Hydrometeor.*, **4**, 1147–1167, https://doi.org/10.1175/1525-7541(2003)004<1147:TVGPCP>2.0.CO;2.

Alexander, M. A., I. Bladé, M. Newman, J. R. Lanzante, N.-C. Lau, and J. D. Scott, 2002: The atmospheric bridge: The influence of ENSO teleconnections on air–sea interaction over the global oceans. *J. Climate*, **15**, 2205–2231, https://doi.org/10.1175/1520-0442(2002)015<2205:TABTIO>2.0.CO;2.

Allen, J. T., M. K. Tippett, and A. H. Sobel, 2015: Influence of the El Niño/Southern Oscillation on tornado and hail frequency in the United States. *Nat. Geosci.*, **8**, 278–283, https://doi.org/10.1038/ngeo2385.

Bjerknes, J., 1966: A possible response of the atmospheric Hadley circulation to equatorial anomalies of ocean temperature. *Tellus*, **18**, 820–829, https://doi.org/10.3402/tellusa.v18i4.9712.

——, 1969: Atmospheric teleconnections from the equatorial Pacific. *Mon. Wea. Rev.*, **97**, 163–172, https://doi.org/10.1175/1520-0493(1969)097<0163:ATFTEP>2.3.CO;2.

Bogenschutz, P. A., A. Gettelman, C. Hannay, V. E. Larson, R. B. Neale, C. Craig, and C.-C. Chen, 2018: The path to CAM6: Coupled simulations with CAM5.4 and CAM5.5. *Geosci. Model Dev.*, **11**, 235–255, https://doi.org/10.5194/gmd-11-235-2018.

Branstator, G., 1985: Analysis of general circulation model sea-surface temperature anomaly simulations using a linear model. Part I: Forced solutions. *J. Atmos. Sci.*, **42**, 2225–2241, https://doi.org/10.1175/1520-0469(1985)042<2225:AOGCMS>2.0.CO;2.

Cai, W., P. van Rensch, T. Cowan, and H. H. Hendon, 2011: Tele-connection pathways of ENSO and the IOD and the mecha-nisms for impacts on Australian rainfall. *J. Climate*, **24**, 3910–3923, https://doi.org/10.1175/2011JCLI4129.1.

Chen, R., I. R. Simpson, C. Deser, and B. Wang, 2020: Model biases in the simulation of the springtime North Pacific ENSO teleconnection. *J. Climate*, **33**, 9985–10002, https://doi.org/10.1175/JCLI-D-19-1004.1.

Cook, A. R., L. M. Leslie, D. B. Parsons, and J. T. Schaefer, 2017: The impact of El Niño–Southern Oscillation (ENSO) on win-ter and early spring U.S. tornado outbreaks. *J. Appl. Meteor. Climatol.*, **56**, 2455–2478, https://doi.org/10.1175/JAMC-D-16-0249.1.

Danabasoglu, G., and Coauthors, 2020: The Community Earth System Model version 2 (CESM2). *J. Adv. Model. Earth Syst.*, **12**, https://doi.org/10.1029/2019MS001916.

Dee, D. P., and Coauthors, 2011: The ERA-Interim reanalysis: Configuration and performance of the data assimilation sys-tem. *Quart. J. Roy. Meteor. Soc.*, **137**, 553–597, https://doi.org/10.1002/qj.828.

Deser, C., I. R. Simpson, K. A. McKinnon, and A. S. Phillips, 2017: The Northern Hemisphere extratropical atmospheric circulation response to ENSO: How well do we know it and how do we evaluate models accordingly? *J. Climate*, **30**, 5059–5082, https://doi.org/10.1175/JCLI-D-16-0844.1.

——, ——, A. S. Phillips, and K. A. McKinnon, 2018: How well do we know ENSO's climate impacts over North America, and how do we evaluate models accordingly? *J. Climate*, **31**, 4991–5014, https://doi.org/10.1175/JCLI-D-17-0783.1.

Domeisen, D. I., C. I. Garfinkel, and A. H. Butler, 2019: The teleconnection of El Niño Southern Oscillation to the stratosphere. *Rev. Geophys.*, **57**, 5–47, https://doi.org/10.1029/2018RG000596.

Ghil, M., and K. Mo, 1991: Intraseasonal oscillations in the global atmosphere. Part II: Southern Hemisphere. *J. Atmos. Sci.*, **48**, 780–790, https://doi.org/10.1175/1520-0469(1991)048<0780:IOITGA>2.0.CO;2.

Harada, Y., and Coauthors, 2016: The JRA-55 reanalysis: Repre-sentation of atmospheric circulation and climate variability. *J. Meteor. Soc. Japan*, **94**, 269–302, https://doi.org/10.2151/jmsj.2016-015.

Held, I. M., and I.-S. Kang, 1987: Barotropic models of the extratropi-cal response to El Niño. *J. Atmos. Sci.*, **44**, 3576–3586, https://doi.org/10.1175/1520-0469(1987)044<3576:BMOTER>2.0.CO;2.

——, S. W. Lyons, and S. Nigam, 1989: Transients and the extratrop-ical response to El Niño. *J. Atmos. Sci.*, **46**, 163–174, https://doi.org/10.1175/1520-0469(1989)046<0163:TATERT>2.0.CO;2.

——, M. Ting, and H. Wang, 2002: Northern winter stationary waves: Theory and modeling. *J. Climate*, **15**, 2125–2144, https://doi.org/10.1175/1520-0442(2002)015<2125:NWSWTA>2.0.CO;2.

Herceg-Bulić, I., and F. Kucharski, 2012: Delayed ENSO impact on spring precipitation over North/Atlantic European region. *Climate Dyn.*, **38**, 2593–2612, https://doi.org/10.1007/s00382-011-1151-9.

——, B. Mezzina, F. Kucharski, P. Ruggieri, and M. P. King, 2017: Wintertime ENSO influence on late spring European climate: The stratospheric response and the role of North Atlantic SST. *Int. J. Climatol.*, **37**, 87–108, https://doi.org/10.1002/joc.4980.

Hersbach, H., and Coauthors, 2020: The ERA5 global reanalysis. *Quart. J. Roy. Meteor. Soc.*, **146**, 1999–2049, https://doi.org/10.1002/qj.3803.

Horel, J. D., and J. M. Wallace, 1981: Planetary-scale atmo-spheric phenomena associated with the southern oscillation. *Mon. Wea. Rev.*, **109**, 813–829, https://doi.org/10.1175/1520-0493(1981)109<0813:PSAPAW>2.0.CO;2.

Hurrell, J. W., 1995: Transient eddy forcing of the rotational flow during northern winter. *J. Atmos. Sci.*, **52**, 2286–2301, https://doi.org/10.1175/1520-0469(1995)052<2286:TEFOTR>2.0.CO;2.

Jong, B.-T., M. Ting, and R. Seager, 2016: El Niño's impact on California precipitation: Seasonality, regionality, and El Niño intensity. *Environ. Res. Lett.*, **11**, 054021, https://doi.org/10.1088/1748-9326/11/5/054021.

——, ——, ——, and W. B. Anderson, 2020: ENSO teleconnec-tions and impacts on U.S. summertime temperature during a multiyear La Niña life cycle. *J. Climate*, **33**, 6009–6024, https://doi.org/10.1175/JCLI-D-19-0701.1.

Kalnay, E., and Coauthors, 1996: The NCEP/NCAR 40-Year Reanalysis Project. *Bull. Amer. Meteor. Soc.*, **77**, 437–471, https://doi.org/10.1175/1520-0477(1996)077<0437:TNYRP>2.0.CO;2.

Karoly, D. J., 1989: Southern Hemisphere circulation features asso-ciated with El Niño–Southern Oscillation events. *J. Climate*, **2**, 1239–1252, https://doi.org/10.1175/1520-0442(1989)002<1239:SHCFAW>2.0.CO;2.

Kay, J. E., and Coauthors, 2015: The Community Earth System Model (CESM) large ensemble project: A community re-source for studying climate change in the presence of internal climate variability. *Bull. Amer. Meteor. Soc.*, **96**, 1333–1349, https://doi.org/10.1175/BAMS-D-13-00255.1.

Kim, H., Y. Zhou, and M. Alexander, 2019: Changes in atmo-spheric rivers and moisture transport over the northeast Pacific and western North America in response to ENSO diversity. *Climate Dyn.*, **52**, 7375–7388, https://doi.org/10.1007/s00382-017-3598-9.

Kobayashi, S., and Coauthors, 2015: The JRA-55 reanalysis: General specifications and basic characteristics. *J. Meteor. Soc. Japan*, **93**, 5–48, https://doi.org/10.2151/jmsj.2015-001.

Kumar, A., and M. P. Hoerling, 1998: Annual cycle of Pacific–North American seasonal predictability associated with dif-ferent phases of ENSO. *J. Climate*, **11**, 3295–3308, https://doi.org/10.1175/1520-0442(1998)011<3295:ACOPNA>2.0.CO;2.

Lau, N.-C., and M. J. Nath, 1994: A modeling study of the relative roles of tropical and extratropical SST anomalies in the vari-ability of the global atmosphere–ocean system. *J. Climate*, **7**, 1184–1207, https://doi.org/10.1175/1520-0442(1994)007<1184:AMSOTR>2.0.CO;2.

——, and ——, 2003: Atmosphere–ocean variations in the Indo-Pacific sector during ENSO episodes. *J. Climate*, **16**, 3–20,

https://doi.org/10.1175/1520-0442(2003)016<0003:AOVITI>2.0.CO;2.

Lehner, F., C. Deser, I. R. Simpson, and L. Terray, 2018: Attributing the U.S. Southwest's recent shift into drier conditions. *Geophys. Res. Lett.*, **45**, 6251–6261, https://doi.org/10.1029/2018GL078312.

L'Heureux, M. L., and D. W. J. Thompson, 2006: Observed relationships between the El Niño–Southern Oscillation and the extratropical zonal-mean circulation. *J. Climate*, **19**, 276–287, https://doi.org/10.1175/JCLI3617.1.

Lyon, B., and A. G. Barnston, 2005: ENSO and the spatial extent of interannual precipitation extremes in tropical land areas. *J. Climate*, **18**, 5095–5109, https://doi.org/10.1175/JCLI3598.1.

McPhaden, M. J., S. E. Zebiak, and M. H. Glantz, 2006: ENSO as an integrating concept in Earth science. *Science*, **314**, 1740–1745, https://doi.org/10.1126/science.1132588.

Neale, R. B., and Coauthors, 2012: Description of the NCAR Community Atmosphere Model (CAM 5.0). NCAR Tech. Rep NCAR/TN-486+STR, 289 pp., https://doi.org/10.5065/wgtk-4g06.

Poli, P., and Coauthors, 2016: ERA-20C: An atmospheric reanalysis of the twentieth century. *J. Climate*, **29**, 4083–4097, https://doi.org/10.1175/JCLI-D-15-0556.1.

Ropelewski, C. F., and M. S. Halpert, 1986: North American precipitation and temperature patterns associated with the El Niño/Southern Oscillation (ENSO). *Mon. Wea. Rev.*, **114**, 2352–2362, https://doi.org/10.1175/1520-0493(1986)114<2352:NAPATP>2.0.CO;2.

Saha, S., and Coauthors, 2010: The NCEP Climate Forecast System Reanalysis. *Bull. Amer. Meteor. Soc.*, **91**, 1015–1058, https://doi.org/10.1175/2010BAMS3001.1.

Sardeshmukh, P. D., and B. J. Hoskins, 1988: The generation of global rotational flow by steady idealized tropical divergence. *J. Atmos. Sci.*, **45**, 1228–1251, https://doi.org/10.1175/1520-0469(1988)045<1228:TGOGRF>2.0.CO;2.

Schmidt, N., E. K. Lipp, J. B. Rose, and M. E. Luther, 2001: ENSO influences on seasonal rainfall and river discharge in Florida. *J. Climate*, **14**, 615–628, https://doi.org/10.1175/1520-0442(2001)014<0615:EIOSRA>2.0.CO;2.

Seager, R., N. Harnik, Y. Kushnir, W. Robinson, and J. Miller, 2003: Mechanisms of hemispherically symmetric climate variability. *J. Climate*, **16**, 2960–2978, https://doi.org/10.1175/1520-0442(2003)016<2960:MOHSCV>2.0.CO;2.

Simmons, A. J., J. M. Wallace, and G. W. Branstator, 1983: Barotropic wave propagation and instability, and atmospheric teleconnection patterns. *J. Atmos. Sci.*, **40**, 1363–1392, https://doi.org/10.1175/1520-0469(1983)040<1363:BWPAIA>2.0.CO;2.

Smith, T. M., R. W. Reynolds, T. C. Peterson, and J. Lawrimore, 2008: Improvements to NOAA's historical merged land–ocean surface temperature analysis (1880–2006). *J. Climate*, **21**, 2283–2296, https://doi.org/10.1175/2007JCLI2100.1.

Spencer, H., and J. M. Slingo, 2003: The simulation of peak and delayed ENSO teleconnections. *J. Climate*, **16**, 1757–1774, https://doi.org/10.1175/1520-0442(2003)016<1757:TSOPAD>2.0.CO;2.

Thirumalai, K., P. N. DiNezio, Y. Okumura, and C. Deser, 2017: Extreme temperatures in Southeast Asia caused by El Niño and worsened by global warming. *Nat. Commun.*, **8**, 15 531, https://doi.org/10.1038/ncomms15531.

Ting, M., and I. M. Held, 1989: The stationary wave response to a tropical SST anomaly in an idealized GCM. *J. Atmos. Sci.*, **47**, 2546–2566, https://doi.org/10.1175/1520-0469(1990)047<2546:TSWRTA>2.0.CO;2.

——, and P. D. Sardeshmukh, 1993: Factors determining the extratropical response to equatorial diabatic heating anomalies. *J. Atmos. Sci.*, **50**, 907–918, https://doi.org/10.1175/1520-0469(1993)050<0907:FDTERT>2.0.CO;2.

——, and L. Yu, 1998: Steady response to tropical heating in wavy linear and nonlinear baroclinic models. *J. Atmos. Sci.*, **55**, 3565–3582, https://doi.org/10.1175/1520-0469(1998)055<3565:SRTTHI>2.0.CO;2.

Trenberth, K. E., G. W. Branstator, D. Karoly, A. Kumar, N.-C. Lau, and C. Ropelewski, 1998: Progress during TOGA in understanding and modeling global teleconnections associated with tropical sea surface temperatures. *J. Geophys. Res.*, **103**, 14 291–14 324, https://doi.org/10.1029/97JC01444.

——, J. M. Caron, D. P. Stepaniak, and S. Worley, 2002: Evolution of El Niño–Southern Oscillation and global atmospheric surface temperatures. *J. Geophys. Res. Atmos.*, **107**, 4065, https://doi.org/10.1029/2000JD000298.

Wang, B., R. Wu, and X. Fu, 2000: Pacific–East Asian teleconnection: How does ENSO affect East Asian climate? *J. Climate*, **13**, 1517–1536, https://doi.org/10.1175/1520-0442(2000)013<1517:PEATHD>2.0.CO;2.

Wolter, K., R. M. Dole, and C. A. Smith, 1999: Short-term climate extremes over the continental United States and ENSO. Part I: Seasonal temperatures. *J. Climate*, **12**, 3255–3272, https://doi.org/10.1175/1520-0442(1999)012<3255:STCEOT>2.0.CO;2.

Wu, R., and B. P. Kirtman, 2005: Roles of Indian and Pacific Ocean air–sea coupling in tropical atmospheric variability. *Climate Dyn.*, **25**, 155–170, https://doi.org/10.1007/s00382-005-0003-x.

Zhang, R., A. Sumi, and M. Kimoto, 1996: Impact of El Niño on the East Asian monsoon. *J. Meteor. Soc. Japan*, **74**, 49–62, https://doi.org/10.2151/jmsj1965.74.1_49.